

Higher-Order Discontinuous Finite Element Discretization for S_N Transport on Arbitrary Polygonal Grids

Michael W. Hackemack^{*,a}, Jean C. Ragusa^b

^a*Knolls Atomic Power Laboratory, P.O. Box 1072, Schenectady, NY 12301, USA*

^b*Department of Nuclear Engineering, Texas A&M University, College Station, TX 77843, USA*

Abstract

In this paper, we analyze the S_N transport equation on arbitrary polygonal grids with a higher-order discontinuous finite element (DFEM) discretization using the quadratic serendipity space of functions. The quadratic functions are constructed from products of the linear Generalized Barycentric Coordinates (GBC) that are compatible with polygonal mesh elements. They span the $\{1, x, y, x^2, xy, y^2\}$ space of functions and they grow by $2n$ on a mesh element where n is the number of the polygon's vertices. Numerical tests confirm that the functions capture exactly quadratic solutions and appropriate convergence rates are observed, including a test case involving spatial adaptive mesh refinement. Finally, the functions are analyzed on diffusive problems and they are confirmed to capture the thick diffusion limit.

Key words: Radiation Transport, Arbitrary Polygonal Grids, Discontinuous Finite Element, Higher-Order Basis Functions

1. Introduction

The solution of the radiation transport equation is important for the fields of reactor physics, high density energy physics, astrophysics, medical imaging and treatment, and others. High-fidelity solutions are difficult to obtain because of the large phase space of the radiation distribution: three for space, two for angular direction on the unit sphere, one for energy, and possibly one for time [1]. The angular flux solution of the radiation transport equation, $\psi(\vec{r}, \vec{\Omega}, E)$, about position \vec{r} , about energy E , and traveling in a cone about direction $\vec{\Omega}$ is given by

*Corresponding author

Email addresses: michael.hackemack@unnpp.gov (Michael W. Hackemack), jean.ragusa@tamu.edu (Jean C. Ragusa)

$$\begin{aligned} \vec{\Omega} \cdot \vec{\nabla} \psi(\vec{r}, \vec{\Omega}, E) + \sigma_t(\vec{r}, E) \psi(\vec{r}, \vec{\Omega}, E) &= Q(\vec{r}, \vec{\Omega}, E) \\ + \int_0^\infty dE' \int_{4\pi} d\Omega' \sigma_s(\vec{r}, \vec{\Omega}' \rightarrow \vec{\Omega}, E' \rightarrow E) \psi(\vec{r}, \vec{\Omega}', E'), \end{aligned} \quad (1)$$

where σ_t and σ_s are the total and scattering cross sections, Q is an angularly-dependent distributed source, and we have omitted temporal dependence. Many different methods have been developed to appropriately discretize Eq. (1) in space, energy, and angle.

In this work, we focus on using solution techniques based on the first-order form of the transport equation. Namely, we use the discrete ordinates (S_N) approximation in angle and the discontinuous Galerkin finite element method (DGFEM) in space. The DFEM discretization of the S_N transport equation dates back to Reed and Hill [2] as well as Lesaint and Raviart [3]. It has been a popular discretization of the transport equation because it is amenable to efficient iterative techniques [4] and scales well on massively parallel architectures [5]. Most of the DGFEM S_N codes use linear functions on simplicial (triangles and tetrahedra) and tensor (quadrilaterals and hexahedra) grids, including DENOVO [6], PARTISN [7], and ATTLA [8]. NEWT [9] and PDT [5] use linear functions, but solve the transport equation on unstructured polytope grids in 2D and 2D/3D, respectively.

For the most part, only linear basis functions have commonly been employed with the DFEM transport equation as the researchers wanted to focus on accuracy in the thick diffusive limit and the robustness of the spatial discretization. The thick diffusion limit is an important asymptotic limit of the transport equation that requires the use of spatial discretizations with certain properties [10]. Even though most work has been done on linear functions, other work has been performed previously on higher-order spatial approximations. For the DFEM transport equation, the TRIPLET code [11] used the Lagrange elements on triangles and Wang and Ragusa [12, 13] used hierarchical triangular elements. Other methods besides the DFEM discretization have utilized higher-order approximations including AHOT for nodal and characteristic transport [14, 15] and Wachspress' functions for curved mesh cell boundaries [16].

In this paper, we seek to analyze the DFEM S_N transport equation with a higher-order spatial discretization on arbitrary polygonal grids. We can summarize the benefits of using polygonal meshes as the following:

1. Polygonal mesh cells are now being employed in other physics communities - notably computational fluid dynamics (CFD) [17] and solid mechanics [18];
2. They can reduce cell/face counts which can reduce algorithm wallclock times depending on the solution method;
3. They can allow for transition elements between different portions of the domain (e.g., triangular elements bordering quadrilateral elements at the border of the boundary layer);

4. They can easily be split along cut planes - allowing the mesh to be partitioned into regular or irregular divisions as well as be generated by simplicial meshing techniques across processor sets in parallel;
5. Hanging nodes from non-conforming meshes, like those that naturally arise from locally refined/adapted meshes using spatial adaptive mesh refinement (AMR) as seen in Figure 1, are not necessary.

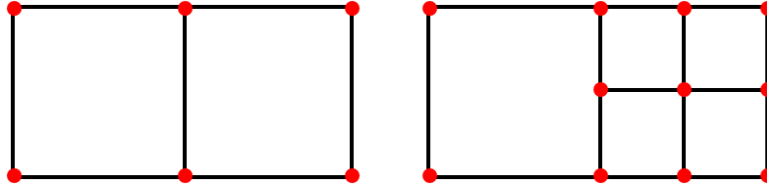


Figure 1: Local mesh refinement of an initial quadrilateral cell (left) leads to a degenerate pentagonal cell (right) without the use of a hanging node.

The higher-order discretization that we employ uses the quadratic serendipity space of functions developed by Rand et al. [19]. They proposed a process where appropriate linear functions, compatible with polygonal mesh elements, are converted into a quadratic space of functions through pairwise products that span $\{1, x, y, x^2, xy, y^2\}$ on strictly-convex polygons. We summarize their process in this work, and provide our methodology that is compatible with weakly-convex polygons (*i.e.*, collinear vertices) so that we could perform AMR calculations using degenerate polygons without hanging nodes. Finally, we note that the functions presented in this work are not solely compatible with just the first-order form of the transport equation. These quadratic serendipity functions can be used with alternative transport equation discretizations, including the self-adjoint angular flux (SAAF) equation, least squares (LS) equation, and even parity (EP) equation [20, 21, 22], for use in codes such as EVENT [23] and RATTLESNAKE [24].

The remainder of the paper is as follows. We provide a brief description of the DGFEM S_N transport equation along with its theoretical spatial convergence rate in Section 2. We then describe a family of functions that are linearly-complete on polygons in Section 3. We then present in Section 4 the methodology to convert the linear polygonal basis functions presented in Section 3 into a serendipity space of basis functions with quadratic-completeness. Section 5 briefly describes the methodology that will be employed to perform spatial AMR with the DGFEM transport equation. Finally, Section 6 provides a set of numerical experiments to verify the polynomial interpolation of the functions as well as their ability to be employed with the transport thick diffusion limit.

2. The DGFEM S_N Discretization of the Transport Equation

In this section, we review the DGFEM S_N transport equation. Given an angular quadrature set, $\{\vec{\Omega}_m, w_m\}_{m=1}^M$, the monoenergetic S_N transport equation with isotropic scattering is defined within an open, convex spatial domain \mathcal{D} , with boundary, $\partial\mathcal{D}$, as

$$\left(\vec{\Omega}_m \cdot \vec{\nabla} + \sigma_t(\vec{r})\right) \psi_m(\vec{r}) = \frac{\sigma_s(\vec{r})}{4\pi} \phi(\vec{r}) + Q_m(\vec{r}), \quad (2)$$

where $\psi_m(\vec{r}) = \psi(\vec{r}, \vec{\Omega}_m)$ is the angular flux at position \vec{r} and in direction $\vec{\Omega}_m$, ~~σ_t and σ_s are the total and scattering cross sections~~, and Q_m is a distributed source for angle m . The scalar flux is defined as

$$\phi(\vec{r}) = \int_{4\pi} d\Omega \psi(\vec{r}, \vec{\Omega}) \approx \sum_{m=1}^M w_m \psi_m(\vec{r}). \quad (3)$$

We then lay down an unstructured mesh, $\mathbb{T}_h \in \mathbb{R}^d$, over the spatial domain, where d is the spatial dimension of the problem (for this work, $d = 2$). This mesh consists of non-overlapping spatial elements to form a complete union over the entire spatial domain: $\mathcal{D} = \bigcup_{K \in \mathbb{T}_h} K$. The 2D domain is meshed with arbitrary polygonal elements.

As is standard in the discontinuous Galerkin scheme, the angular flux unknown of Eq. (2) is expanded using discontinuous **basis functions**:

$$\psi_m(\vec{r}) \approx \sum_K \sum_{j=1}^{n_K} \psi_{m,j} b_j(\vec{r}). \quad (4)$$

The basis functions are nonzero over a single element and discontinuous across the element interfaces. The DGFEM weak form for the transport equation is obtained by multiplying Eq. (2) by the test function b , integrating over element K , applying the divergence Theorem to the streaming term, and using the standard upwind technique for the angular flux at the element's boundaries. A compact notation for the weak form over element K , for an angular direction $\vec{\Omega}_m$, is as follows:

$$\begin{aligned} & \left\langle (\vec{\Omega}_m \cdot \vec{n}) b, \psi_m \right\rangle_{\partial K^+} - \left(\vec{\Omega}_m \cdot \vec{\nabla} b, \psi_m \right)_K + \left(\sigma_t b, \psi_m \right)_K \\ & = \left(\frac{\sigma_s}{4\pi} b, \phi \right)_K + (b, Q_m)_K - \left\langle (\vec{\Omega}_m \cdot \vec{n}) b, \psi_m^\uparrow \right\rangle_{\partial K^-}. \end{aligned} \quad (5)$$

In Eq. (5), ∂K^\pm represents the ~~inflow/outflow~~ boundary of element K (with respect to direction $\vec{\Omega}_m$),

$$\partial K^\pm = \left\{ \vec{r} \in \partial K \mid \vec{\Omega}_m \cdot \vec{n}_K(\vec{r}) \gtrless 0 \right\}, \quad (6)$$

with $\vec{n}_K(\vec{r})$ the outward unit normal vector at location \vec{r} , ψ_m^\uparrow are the angular flux values on an inflow face taken from the upwind neighbor element, and the inner products

$$(u, v)_K \equiv \int_K u v dr \quad \text{and} \quad \langle u, v \rangle_{\partial K} \equiv \int_{\partial K} u v ds \quad (7)$$

correspond to integrations over the cell volume and faces, respectively, where $dr \in \mathbb{R}^d$ is within the cell and $ds \in \mathbb{R}^{d-1}$ is along the cell boundary. In Eq. (5), all angular flux unknowns “live on” element K , except for the upwinded values which are taken from the upwind neighboring element:

$$\psi_m^\uparrow(\vec{r}) = \lim_{s \rightarrow 0^+} \psi_m(\vec{r} + s\vec{n}_K(\vec{r})), \quad \vec{r} \in \partial K^-. \quad (8)$$

The spatial convergence of DGFEM methods for hyperbolic systems has been extensively studied [3, 25, 26, 12]. With the discretized flux solution, $\phi_h \in W_{\mathcal{D}}^h$, corresponding to our unstructured mesh, \mathbb{T}_h , we can define an error for our DGFEM transport solution with the L_2 -norm as

$$\|\phi_h - \phi_{exact}\|_{L_2} \leq C \frac{h^q}{(p+1)^{q-1/2}}. \quad (9)$$

In Eq. (9), $q = \min(p+1, r)$, h is the maximum diameter of all the mesh elements, p is the polynomial completeness of the finite element function space, r is the regularity index of the transport solution, and C is a constant that is independent of the mesh employed. Investigating the q term in Eq. (9), we can see that our DGFEM transport convergence rates are all limited by the regularity, r , of the solution space. If we have sufficiently smooth data, then the exact transport solution belongs, at most, in the $H^{3/2}(\mathcal{D})$ Hilbert space, which yields a solution regularity of $r = 3/2$. However, in the case of a pure absorber or void, the exact transport solution lives in the $H^{1/2}(\mathcal{D})$ Hilbert space, which yields a solution regularity of $r = 1/2$. From these spaces, one would think that the transport solution regularity would impede the use of higher-order finite element spaces. We note, however, that these regularity indices only apply to the asymptotic convergence range, which usually only applies to very fine meshes that are much smaller than typically employed meshes. Therefore, we expect to capture up to order $(p+1)$ convergence in preasymptotic ranges that would be employed for a wide variety of transport problems.

We can also define the DGFEM transport solution convergence rates in terms of the total number of spatial degrees of freedom, N_{dof} , instead of the maximum element diameter, h . We first relate the total number of mesh elements, N_{ele} , to the maximum element diameter: $N_{ele} \propto h^{-d}$, where we assume that the polygonal elements are strictly-convex. We then assume that the finite element functional space on each element is the serendipity space [27]. This means that the number of degrees of freedom per element is proportional to the polynomial order: $N_{dof} \propto p h^{-d}$ or $h \propto \left(\frac{N_{dof}}{p}\right)^{-1/d}$. Substituting this relation into Eq. (9), yields an L_2 -norm convergence rate in terms of the problem’s total number of spatial degrees of freedom,

$$\|\phi_h - \phi_{exact}\|_{L_2} \leq C(p) N_{dof}^{-q/d}, \quad C(p) = \frac{p^{q/d}}{(p+1)^{q-1/2}}. \quad (10)$$

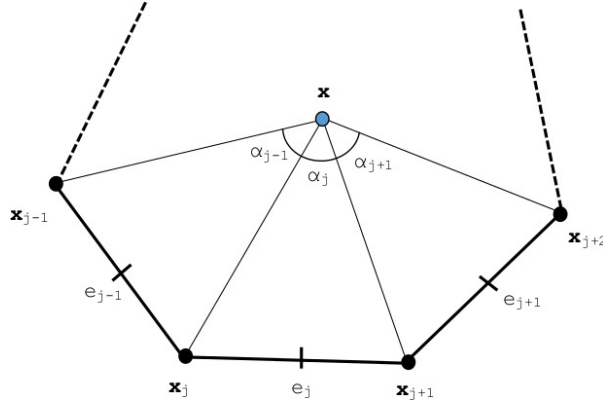


Figure 2: Arbitrary polygon with geometric properties used for 2D basis function generation.

3. Linear Polygonal Basis Functions

We now describe the linear polygonal functions that we will analyze where any geometric descriptions are given by Figure 2. To achieve the maximum possible solution convergence rate of Eq. (9), these functions need to exactly interpolate the $\{1, x, y\}$ span of functions. For this work, we will utilize a family of linear functions known as Generalized Barycentric Coordinates (GBC) [28]. In particular, we investigated the Wachspress functions, the mean value functions, and the maximum entropy functions. These functions (denoted as $\{\lambda_j\}_{j=1}^n$ on a polygon with n vertices) have the following properties:

1. Positivity: $\lambda_j \geq 0$ (convex polygons);
2. Partition of unity: $\sum_{j=1}^n \lambda_j = 1$;
3. Affine combination: $\sum_{j=1}^n \vec{r}_j \lambda_j(\vec{r}) = \vec{r}$;
4. Lagrange property: $\lambda_i(\vec{r}_j) = \delta_{ij}$;
5. Piecewise boundary linearity: $\lambda_j((1 - \mu)\vec{r}_j + \mu\vec{r}_{j+1}) = (1 - \mu)\lambda_j(\vec{r}_j) + \mu\lambda_j(\vec{r}_{j+1})$, $\mu \in [0, 1]$.

We can see from properties 2 and 3 that the GBCs span the $\{1, x, y\}$ space and can exactly interpolate constant and linear functions.

3.1. Wachspress Rational Functions

The first linearly-complete polygonal functions that we will consider are the Wachspress rational functions [29]. These rational functions were the first derived for 2D polygons and possess all the properties of the barycentric functions. However, they are only valid interpolants over strictly-convex polygons. Weakly-convex polygons (containing colinear vertices) lose piecewise linearity on the boundary. Concave polygons have regions within their domain that are

undefined and divide-by-zero occurs. The Wachspress functions (which we denote as λ^W) have the following form

$$\lambda_j^W(\vec{r}) = \frac{w_j(\vec{r})}{\sum_{i=1}^n w_i(\vec{r})}, \quad (11)$$

where the Wachspress weight function for vertex j , w_j , has the following definition:

$$w_j(\vec{r}) = \frac{A(\vec{r}_{j-1}, \vec{r}_j, \vec{r}_{j+1})}{A(\vec{r}, \vec{r}_{j-1}, \vec{r}_j) A(\vec{r}, \vec{r}_j, \vec{r}_{j+1})}. \quad (12)$$

In Eq. (12), the terms $A(\vec{a}, \vec{b}, \vec{c})$ denote the signed area of the triangle with vertices \vec{a} , \vec{b} , and \vec{c} . Each of these signed areas can be computed by

$$A(\vec{a}, \vec{b}, \vec{c}) = \frac{1}{2} \begin{vmatrix} 1 & 1 & 1 \\ x_a & x_b & x_c \\ y_a & y_b & y_c \end{vmatrix}. \quad (13)$$

Through observation of Eq. (12), we can see that the denominator of w_j goes to zero on faces e_j and e_{j+1} . This makes numerical evaluation of the Wachspress functions impossible on the boundary of the element boundary. However, the functions do have valid limits on the boundary, which will be shown in Appendix A.

3.2. Mean Value Functions

The second linearly-complete 2D polygonal functions that we ~~will~~ analyze are the mean value functions (MV) [30]. These functions were derived to approximate harmonic maps on a polygon by a set of piecewise linear maps over a triangulation of the polygon for use in computer aided graphic design. The mean value function at vertex j , λ_j^{MV} , is defined as

$$\lambda_j^{MV}(\vec{r}) = \frac{w_j(\vec{r})}{\sum_{i=1}^n w_i(\vec{r})}, \quad (14)$$

where the mean value weight function for vertex j , w_j , has the following definition:

$$w_j(\vec{r}) = \frac{\tan(\alpha_{j-1}/2) + \tan(\alpha_j/2)}{|\vec{r}_j - \vec{r}|}. \quad (15)$$

Similar to the Wachspress functions, we can observe from Eq. (15) that the numerator of w_j tends to infinity on faces e_j and e_{j+1} as $\alpha_j \rightarrow \pi/2$. Again, the MV functions have valid limits on the boundary as shown in Appendix A.

187 3.3. Maximum Entropy Functions

188 The final linearly-complete 2D polygonal functions that we will analyze are
 189 the maximum entropy functions (ME) [31]. The principle of maximum en-
 190 tropy stems from the concept of Shannon entropy [32], where the maximum of
 191 the Shannon entropy function, H , will lead to the least-biased statistical infer-
 192 ence for some set of testable constraints [33]. For FEM analysis, these testable
 193 constraints are the partition of unity and affine combination properties of the
 194 barycentric functions. For n discrete probability functions (corresponding to
 195 the n vertex functions), the functional form for the Shannon entropy can be
 196 given by

$$H(b, m) = - \sum_{j=1}^n b_j \log \left(\frac{b_j}{m_j} \right), \quad (16)$$

197 where m_j is called the prior distribution. If $(\lambda_j^{ME}(\vec{x}), j = 1, \dots, n)$ is the solution
 198 of the following constrained optimization problem

$$\max_{b(\vec{r})} H(b, m, \vec{r}), \quad (17)$$

199 then the maximum entropy functions can be given by

$$\lambda_j^{ME}(\vec{r}) = \frac{w_j(\vec{r})}{\sum_{i=1}^n w_i(\vec{r})}, \quad (18)$$

200 where the maximum entropy weight function for vertex j , w_j , has the following
 201 definition,

$$w_j(\vec{r}) = m_j(\vec{r}) \exp(-\vec{\kappa} \cdot (\vec{r}_j - \vec{r})), \quad (19)$$

202 and $\vec{\kappa}$ is a vector value of dimension 2 that will be explained shortly. In the
 203 context of Eq. (19), the prior distribution, m_j , can be viewed as a weight
 204 function associated with vertex j . This means that there is variability that one
 205 can employ for these weight functions. For FEM applications, an appropriate
 206 functional form for the prior distribution is given by

$$m_j(\vec{r}) = \frac{\pi_j(\vec{r})}{\sum_{k=1}^n \pi_k(\vec{r})}, \quad (20)$$

207 where

$$\pi_j(\vec{r}) = \prod_{k \neq j-1, j}^n \rho_k(\vec{r}) = \rho_1(\vec{r}) \dots \rho_{j-2}(\vec{r}) \rho_{j+1}(\vec{r}) \dots \rho_n(\vec{r}), \quad (21)$$

208 and

$$\rho_j(\vec{r}) = \|\vec{r} - \vec{r}_j\| + \|\vec{r} - \vec{r}_{j+1}\| - \|\vec{r}_{j+1} - \vec{r}_j\|. \quad (22)$$

Table 1: Summary of the properties of the 2D barycentric functions.

Basis Function	Polygon Type	Evaluation
Wachspress	Convex	Direct
Mean Value	Convex/Concave	Direct
Max Entropy	Convex/Concave	Iterative

In Eqs. (21) and (22), we have defined a new **weight** function, ρ_j , that corresponds to face e_j between vertices j and $j + 1$. These face functions are zero along face e_j , but strictly positive elsewhere due to the triangle inequality. This means that the vertex function, π_j , is also non-negative and vanishes on all faces that are not adjacent to vertex j .

Now that we have provided sufficient details for the basis functions and their weight functions, we can explain how the $\vec{\kappa}$ vector in Eq. (19) is computed. We can see that once $\vec{\kappa}$ is known, the ME functions can be directly calculated. To do this, we solve the constrained optimization problem of Eq. (17) through the use of Lagrange multipliers with a Newton's method. If we define κ_0 as the Lagrange multiplier for the constant constraint, then the Lagrangian for the problem of Eq. (17) is given by

$$\mathcal{L}(\vec{\kappa}; \kappa_0, \vec{\kappa}) = - \sum_{j=1}^n b_j \log \left(\frac{b_j}{m_j} \right) - \kappa_0 \left(\sum_{j=1}^n b_j - 1 \right) - \vec{\kappa} \cdot \left(\sum_{j=1}^n b_j (\vec{r}_j - \vec{r}) \right), \quad (23)$$

where we omitted the spatial parameter \vec{r} for brevity. If we define $W = \sum_{j=1}^n w_j(\vec{r})$, then the solution of Eq. (18) is equivalent to solving the following dual unconstrained optimization problem [34]:

$$\vec{\kappa}^* = \min_{\vec{\kappa}} F(\vec{\kappa}), \quad F(\vec{\kappa}) = \log W(\vec{\kappa}). \quad (24)$$

3.4. Summary of the Linear Polygonal Basis Functions

For this work, we are analyzing **three** different linear barycentric functions for use as our FEM basis functions: the Wachspress rational functions, the mean value functions, and the maximum entropy functions. **Table 1** provides a summary of the properties for the different functions. The MV and ME functions can interpolate degenerate-convex and concave polygons while the Wachspress functions can only interpolate strictly-convex polygons. From just the geometry of the polygon, the Wachspress and MV functions can be directly evaluated, whereas the ME functions require an iterative approach with Newton's method since their functional form constitutes a non-linear optimization problem.

We conclude our discussion of the linear barycentric functions by providing some example contour plots. Figure 3 provides the contour plots of the different functions located at vertex $(0, 1)$ on the unit square. Figure 4 provides the

237 contour plots on the degenerate pentagon that is formed by inserting a vertex at
 238 $(1/2, 1)$ into the unit square. This re-emphasizes that the Wachspress functions
 239 are only valid interpolatory functions on strongly-convex polygons. Finally,
 240 Figures 5 and 6 provide the contour plots of the MV and ME functions on the
 241 L-shaped domain at the $(0, 1)$ and $(1/2, 1/2)$ vertices, respectively.

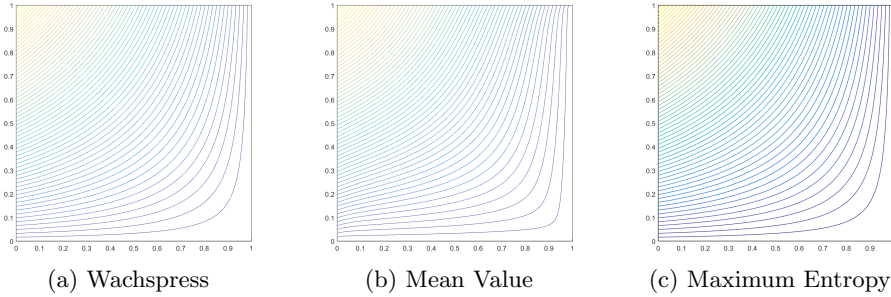


Figure 3: Contour plots of the different linear basis function on the unit square located at vertex $(0,1)$.

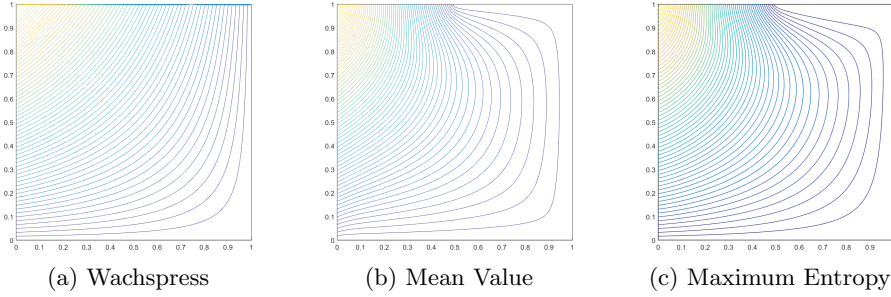


Figure 4: Contour plots of the different linear basis function on the degenerate pentagon located at vertex $(0,1)$. It is clear that the Wachspress functions fail for the weakly convex case.

242 4. Quadratic Serendipity Polygonal Basis Functions

243 We have ~~given complete details~~ on the linearly-complete generalized barycen-
 244 tric functions that ~~we will investigate for this work~~. Now, we describe how to
 245 convert any generalized barycentric function into the quadratic serendipity space
 246 of functions to yield quadratic (not linear) precision based on the work of Rand
 247 et al. [19]. ~~The maximum entropy functions were independently converted into~~
 248 ~~the quadratic space [35, 36]. These 2D serendipity functions can exactly inter-~~
 249 ~~polate the $\{1, x, y, x^2, xy, y^2\}$ span of functions.~~

250 Now, we give the full details on converting the linear generalized barycentric
 251 functions to the quadratic serendipity space of functions. Figure 7 gives a visual

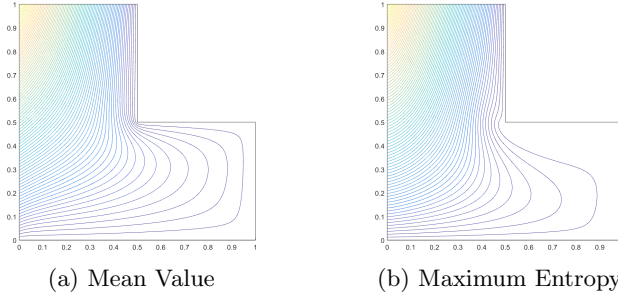


Figure 5: Contour plots of the mean value and maximum entropy functions on the L-shaped domain at vertex $(0, 1)$.

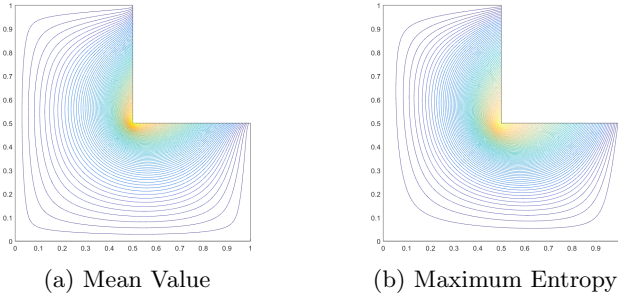


Figure 6: Contour plots of the mean value and maximum entropy functions on the L-shaped domain at vertex $(1/2, 1/2)$.

252 depiction of this conversion process. For a polygon with n vertices, we can
 253 summarize this procedure as the following:

- 254 1. For a point \vec{r} , compute the n linear barycentric functions $\{\lambda_i(\vec{r})\}$ (e.g.,
 255 Wachspress, mean value, or maximum entropy);
- 256 2. Take all non-repeating pairwise products of the linear functions to obtain
 257 $\frac{n(n+1)}{2}$ quadratic functions $\{\mu_{ab}\}$;
- 258 3. Form the linear transformation matrix \mathbb{A} through the use of monomial
 259 constraint equations;
- 260 4. Use the \mathbb{A} matrix to reduce the $\{\mu_{ab}\}$ function set to the $2n$ serendipity
 261 basis set $\{\xi_{ij}\}$;
- 262 5. (Optional) Use the \mathbb{L} matrix to convert $\{\xi_{ij}\}$ to the Lagrange basis: $\{\chi_{ij}\}$
 263 (Appendix B).

264 We begin by computing the $(i = 1, \dots, n)$ linear barycentric functions, $\{\lambda_i(\vec{r})\}$,
 265 and their gradients, $\{\vec{\nabla}\lambda_i(\vec{r})\}$, for a point \vec{r} . These linearly-complete barycen-
 266 tric functions can be converted immediately to barycentric-like functions with
 267 quadratic precision. Taking all non-repeating pairwise products of the linear
 268 functions yields a total of $N_Q = \frac{n(n+1)}{2}$ quadratic functions: $\mu_{ab} = \lambda_a \lambda_b$. Do-
 269 ing this generates functions that either live on the polygon's vertices, mid-face

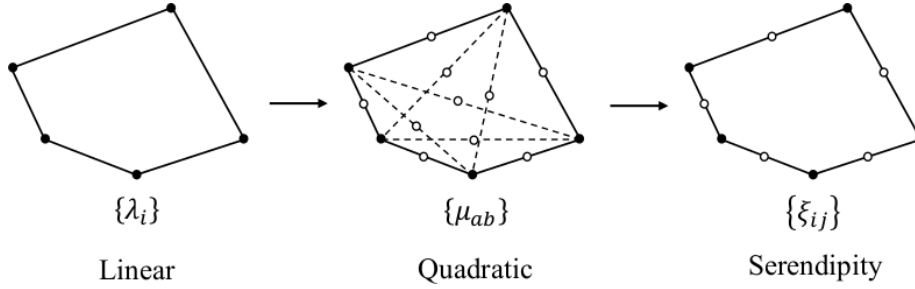


Figure 7: Overview of the process to construct the quadratic serendipity basis functions on polygons. The filled dots correspond to basis functions that maintain the Lagrange property while empty dots do not.

points, or midpoints of the polygon's diagonals between two vertices as seen in Figure 7. The n vertex functions are denoted as $ab \in V$ ($a = b$), the n mid-face (mid-edge) functions are denoted as $ab \in E$ ($|a - b| = 1$), and the $\frac{n(n-3)}{2}$ diameter (interior) functions are denoted as $ab \in D$ ($|a - b| > 1$). For the mid-edge and interior functions, only 1 combination of ab is kept since $\mu_{ab} = \mu_{ba}$. We also define the abbreviated notation of $\vec{r}_{ab} = \frac{\vec{r}_a + \vec{r}_b}{2}$, so that \vec{r}_{aa} corresponds to a vertex function at \vec{r}_a . Using these various notations, we can write the precision properties of the μ_{ab} functions for the constant constraint,

$$\sum_{aa \in V} \mu_{aa}(\vec{r}) + \sum_{ab \in E \cup D} 2\mu_{ab}(\vec{r}) = 1, \quad (25)$$

for the linear constraint,

$$\sum_{aa \in V} \mu_{aa}(\vec{r}) \vec{r}_{aa} + \sum_{ab \in E \cup D} 2\mu_{ab}(\vec{r}) \vec{r}_{ab} = \vec{r}, \quad (26)$$

and for the quadratic constraint,

$$\sum_{aa \in V} \mu_{aa}(\vec{r}) (\vec{r}_a \otimes \vec{r}_a) + \sum_{ab \in E \cup D} \mu_{ab}(\vec{r}) (\vec{r}_a \otimes \vec{r}_b + \vec{r}_b \otimes \vec{r}_a) = \vec{r} \otimes \vec{r}. \quad (27)$$

In Eq. (27), \otimes is the dyadic tensor product. We can immediately see that quadratic precision is ensured. However, the set of these pairwise quadratic functions grows quadratically. This means that as n grows large, the number of interpolatory functions grows as order $O(n^2)$, but still only maintains precision of the $\{1, x, y, x^2, xy, y^2\}$ space of functions. Therefore, the computational work required to utilize these quadratic barycentric functions can become prohibitive for polygons with large vertex counts.

To minimize the number of interpolatory functions but still maintain the precision of the $\{1, x, y, x^2, xy, y^2\}$ span of functions, we seek to convert the quadratic barycentric functions into the quadratic serendipity space of functions $\{\xi_{ij}\}$. This quadratic serendipity space only contains the vertex and mid-face

functions (total of $2n$) and has been extensively studied for tensor-based elements in the past [27]. This means that we seek to reduce the $\{\mu_{ab}\}$ set of functions by removing the ~~diagonal~~ functions ($ab \in D$) while still maintaining quadratic precision. If we define ξ_{ii} and $\xi_{i(i+1)}$ as the serendipity functions that live at vertex i and the mid-face point between vertices i and $i+1$, respectively, then we can write the serendipity precision properties for the constant constraint,

$$\sum_{ii \in V} \xi_{ii}(\vec{r}) + \sum_{i(i+1) \in E} 2\xi_{i(i+1)}(\vec{r}) = 1, \quad (28)$$

for the linear constraint,

$$\sum_{ii \in V} \xi_{ii}(\vec{r}) \vec{r}_{ii} + \sum_{i(i+1) \in E} 2\xi_{i(i+1)}(\vec{r}) \vec{r}_{i(i+1)} = \vec{r}, \quad (29)$$

and for the quadratic constraint,

$$\sum_{ii \in V} \xi_{ii}(\vec{r}) (\vec{r}_i \otimes \vec{r}_i) + \sum_{i(i+1) \in E} \xi_{i(i+1)}(\vec{r}) (\vec{r}_i \otimes \vec{r}_{i+1} + \vec{r}_{i+1} \otimes \vec{r}_i) = \vec{r} \otimes \vec{r}. \quad (30)$$

To remove the ~~diagonal~~ functions, we formalize this procedure by recasting it as a linear algebra problem. We seek a matrix \mathbb{A} such that the linear transformation,

$$\{\xi\} = \mathbb{A} \{\mu\}, \quad (31)$$

will satisfy the precision properties of Eqs. (28 - 30). It is easy to see that \mathbb{A} has dimension $(2n \times N_Q)$. We wish for this matrix to have constant entries for any point within the polygon's interior so that it does not have to be recalculated for each interpolatory point of interest. To ease the notation, we will assign specific basis orderings for the quadratic and quadratic serendipity functions. The serendipity basis is ordered such that all vertex functions ($ii \in V$) in a counter-clockwise ordering are first, followed by a counter-clockwise ordering of the mid-face nodes ($ij \in E$) starting with the node between vertices 1 and 2. This ordering can be succinctly stated by

$$\{\xi_{ij}\} = \left\{ [\xi_{11}, \xi_{22}, \dots, \xi_{nn}], [\xi_{12}, \xi_{23}, \dots, \xi_{(n-1)n}, \xi_{n(n+1)}] \right\}, \quad (32)$$

where $n+1 \rightarrow 1$. The quadratic basis begins identically to the serendipity basis by first listing the vertex and mid-face functions. Then the ~~diagonal~~ functions are indexed in lexicographical order. This gives the following ordering for the quadratic functions

$$\{\mu_{ab}\} = \left\{ [\mu_{11}, \mu_{22}, \dots, \mu_{nn}], [\mu_{12}, \mu_{23}, \dots, \mu_{(n-1)n}, \mu_{n(n+1)}], [\mu_{13}, \dots, (\text{lexicographical}), \dots, \mu_{(n-2)n}] \right\}. \quad (33)$$

316 With these basis orderings, we can now denote the entries of \mathbb{A} (given by c_{ab}^{ij})
 317 as

$$\mathbb{A} = \begin{bmatrix} c_{11}^{11} & \dots & c_{ab}^{11} & \dots & c_{(n-2)n}^{11} \\ \vdots & \ddots & \vdots & \ddots & \vdots \\ c_{11}^{ij} & \dots & c_{ab}^{ij} & \dots & c_{(n-2)n}^{ij} \\ \vdots & \ddots & \vdots & \ddots & \vdots \\ c_{11}^{n(n+1)} & \dots & c_{ab}^{n(n+1)} & \dots & c_{(n-2)n}^{n(n+1)} \end{bmatrix}, \quad (34)$$

318 A sufficient set of constraints for the entries in \mathbb{A} to ensure the precision
 319 properties of Eqs. (28 - 30) can be written for the constant constraint,

$$\begin{aligned} \sum_{ii \in V} c_{aa}^{ii} + \sum_{i(i+1) \in E} 2c_{aa}^{i(i+1)} &= 1, & \forall aa \in V \\ \sum_{ii \in V} c_{ab}^{ii} + \sum_{i(i+1) \in E} 2c_{ab}^{i(i+1)} &= 2, & \forall ab \in E \cup D \end{aligned} \quad (35)$$

320 for the linear constraint,

$$\begin{aligned} \sum_{ii \in V} c_{aa}^{ii} \vec{r}_{ii} + \sum_{i(i+1) \in E} 2c_{aa}^{i(i+1)} \vec{r}_{i(i+1)} &= \vec{r}_{aa}, & \forall aa \in V \\ \sum_{ii \in V} c_{ab}^{ii} \vec{r}_{ii} + \sum_{i(i+1) \in E} 2c_{ab}^{i(i+1)} \vec{r}_{i(i+1)} &= 2\vec{r}_{ab}, & \forall ab \in E \cup D \end{aligned} \quad (36)$$

321 for the $a \in V$ vertex quadratic constraints

$$\sum_{ii \in V} c_{aa}^{ii} \vec{r}_{ii} \otimes \vec{r}_{ii} + \sum_{i(i+1) \in E} c_{aa}^{i(i+1)} (\vec{r}_i \otimes \vec{r}_{i+1} + \vec{r}_{i+1} \otimes \vec{r}_i) = \vec{r}_{aa} \otimes \vec{r}_{aa}, \quad (37)$$

322 and for the $ab \in E \cup D$ mid-face and ~~diagonal~~ quadratic constraints,

$$\sum_{ii \in V} c_{ab}^{ii} \vec{r}_{ii} \otimes \vec{r}_{ii} + \sum_{i(i+1) \in E} c_{ab}^{i(i+1)} (\vec{r}_i \otimes \vec{r}_{i+1} + \vec{r}_{i+1} \otimes \vec{r}_i) = (\vec{r}_a \otimes \vec{r}_b + \vec{r}_b \otimes \vec{r}_a). \quad (38)$$

323 For $n > 3$, there are more coefficients than the six constraint equations. This
 324 means that there is flexibility in the construction of the solution to the constraint
 325 equations. Therefore, we choose a simple structure for \mathbb{A} that consists of the
 326 following,

$$\mathbb{A} = [\mathbb{I} \mid \mathbb{A}'], \quad (39)$$

327 where \mathbb{I} is the $(2n \times 2n)$ identity matrix, and \mathbb{A}' is a full $(2n \times \frac{n(n-3)}{2})$ matrix. This
 328 means that the vertex and face midpoint serendipity functions, ξ_{ij} , are formed
 329 by taking their corresponding quadratic function, μ_{ij} , and adding some linear

330 combination of the interior functions. Therefore, we only need to determine the
 331 $\frac{n(n-3)}{2}$ columns of the \mathbb{A}' matrix to complete this linear transformation.

332 In their work, Rand et al. proposed a methodology where only six coefficients
 333 are chosen to be non-zero and can be directly calculated through geometric
 334 expressions. However, their approach is only valid for strictly-convex polygons.
 335 This will not work for our analysis since we wish to also analyze degenerate
 336 polygons that will arise in our AMR calculations. Therefore, we will use a
 337 least squares method to calculate each of the columns of \mathbb{A}' . We note that the
 338 coefficients calculated with this least squares method and that of Rand will be
 339 identical only for rectangles. If we isolate the column (ab) from \mathbb{A}' , then we can
 340 form the following system of equations,

$$\mathbb{B}\vec{c}_{ab} = \vec{q}_{ab}, \quad (40)$$

341 where \mathbb{B} is a matrix of dimension $(6 \times 2n)$, \vec{c}_{ab} is a vector of length $2n$, and \vec{q}_{ab}
 342 is a vector of length 6. The entries of \mathbb{B} correspond to coefficients given in the
 343 left-hand-side terms of Eqs. (35), (36), and (38). The values of \vec{q}_{ab} are given by
 344 the right-hand-side ~~constants~~ of these same equations. To invert \mathbb{B} , we use the
 345 Moore-Penrose pseudoinverse (denoted as \mathbb{B}^*) [37]. For an under-determined
 346 system of equations, the pseudoinverse is given by,

$$\mathbb{B}^* = \mathbb{B}^T (\mathbb{B}\mathbb{B}^T)^{-1}. \quad (41)$$

347 We note that we have only tested this methodology on convex and weakly-
 348 convex polygons. Once all of the coefficients for the \mathbb{A}' matrix are known, each
 349 of the quadratic serendipity functions can be computed by

$$\xi_{ij} = \lambda_i \lambda_j + \sum_{ab \in D} c_{ab}^{ij} \lambda_a \lambda_b, \quad (42)$$

350 where $j = i$ for the vertex functions and $j = i + 1$ for the mid-face functions
 351 ~~(we again note that $n + 1 = 1$).~~ From Eq. (42), we can clearly see that the
 352 quadratic functions, μ_{ab} , act as an intermediate step and do not ever need to
 353 be explicitly computed.

354 We now present some example contour plots of the different quadratic serendipity-
 355 functions. Figures 8 and 9 provide contour plots of the functions on the unit
 356 square at the upper-left vertex and left side-node, respectively. Then, Figures
 357 10 and 11 provide the contour plots of the MV and ME functions on the de-
 358 generate square that is formed by inserting a vertex at $(1/2, 1)$ onto the unit
 359 square.

360 5. Adaptive Mesh Refinement Using Polygonal Basis Functions

361 The use of spatial AMR for the radiation transport equation is ~~in its in-~~
 362 ~~fancy~~ [38, 39, 40, 41]. For this work, we will only utilize h -type refinement strate-
 363 gies for 2D transport problems on initial meshes with only quadrilateral cells.
 364 The AMR procedure begins with an initial and typically coarse mesh. Once this

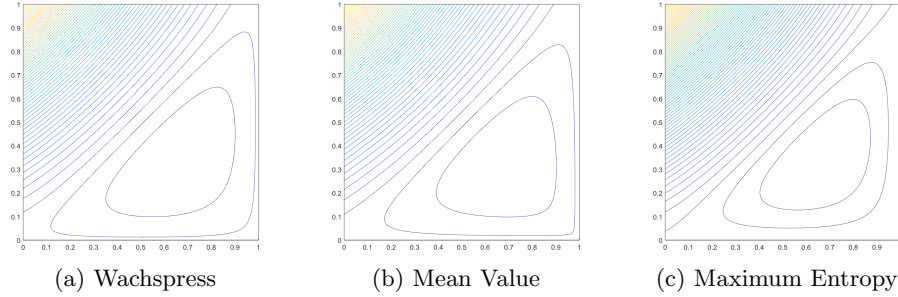


Figure 8: Contour plots of the different quadratic serendipity basis function on the unit square located at vertex $(0,1)$.

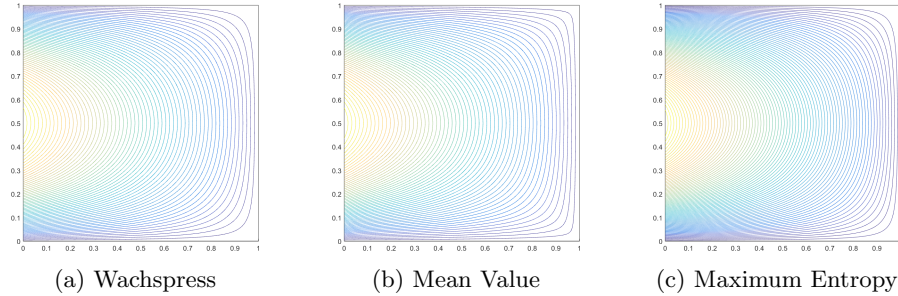


Figure 9: Contour plots of the different quadratic serendipity basis function on the unit square located at vertex $(0,1/2)$.

365 solution is determined, *a posteriori* error estimates are used to determine which
 366 problem regions contain the largest spatial discretization error [42, 43]. Then,
 367 based on some refinement criterion, some subset of mesh elements are flagged
 368 for local refinement. From these flagged elements, the mesh can be refined,
 369 and a new and more accurate solution can further be obtained. This process is
 370 repeated until some global convergence criterion is satisfied or some number of
 371 mesh adaptation cycles are performed.

372 At the heart of the mesh adaptation procedures is the reliance on an ac-
 373 curate estimation of the numerical solution error. The state-of-the-art error
 374 estimators rely on either adjoint-based methods [38, 44, 40] or projection-based
 375 methods [45]. However, these methods require an additional calculation of the
 376 solution at each refinement level in a richer (and more difficult to solve) func-
 377 tional space. Therefore, we will employ a simpler error estimator that does not
 378 require an additional solution calculation. For this work, we will utilize the
 379 jump-based error estimator since it is the most straightforward to define and
 380 execute. The estimate of the error for mesh cell K of the mesh at refinement
 381 level r , \mathbb{T}_h^r , is given by the following,

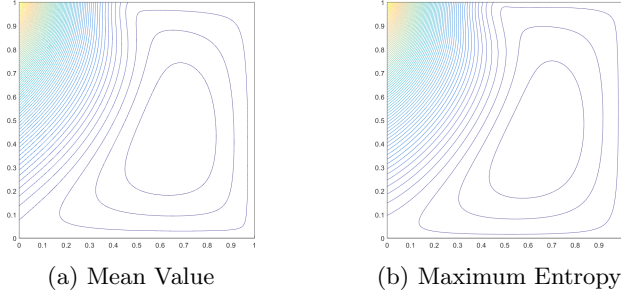


Figure 10: Contour plots of the different quadratic serendipity basis function on the unit degenerate pentagon located at vertex (0,1).

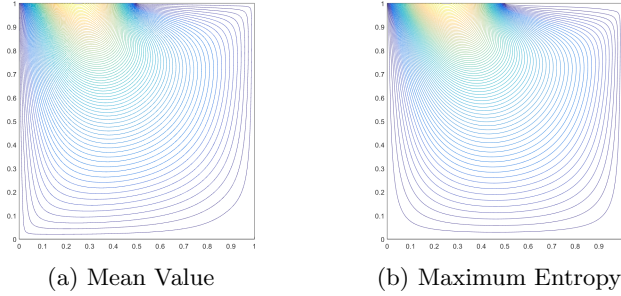


Figure 11: Contour plots of the different quadratic serendipity basis function on the unit degenerate pentagon located at mid-face node (1/4,1).

$$\eta_K^r = \int_{\partial K} \llbracket \phi^r \rrbracket^2 ds = \int_{\partial K} \left(\sum_m w_m \llbracket \psi_m^r \rrbracket \right)^2, \quad (43)$$

382 where $\llbracket \cdot \rrbracket$ is the jump operator along a face defined as,

$$\llbracket \phi(\vec{r}) \rrbracket = \phi^+(\vec{r}) - \phi^-(\vec{r}), \quad (44)$$

383 and the terms, $\phi^+(\vec{r})$ and $\phi^-(\vec{r})$, are subject to the trace:

$$\phi^\pm(\vec{r}) = \lim_{s \rightarrow 0^\pm} \phi(\vec{r} + s\vec{n}). \quad (45)$$

384 In this case, the outward normal, \vec{n} , is determined with respect to the element
 385 K along its boundary, ∂K . With this trace, $\phi^-(\vec{r})$ always corresponds to the
 386 solution within cell K . Investigating face f of cell K , the across-face solution,
 387 $\phi^+(\vec{r})$, is dependent on the boundary type of face f . The across-face solutions
 388 can be succinctly written:

$$\phi^+(\vec{r}) = \begin{cases} \lim_{s \rightarrow 0^+} \phi(\vec{r} + s\vec{n}) & \vec{r} \notin \partial\mathcal{D} \\ \sum_{\vec{\Omega}_m \cdot \vec{n} > 0} \psi_m^-(\vec{r}) + \sum_{\vec{\Omega}_m \cdot \vec{n} < 0} \psi_m^{inc}(\vec{r}) & \vec{r} \in \partial\mathcal{D}^d \\ \phi^-(\vec{r}) & \vec{r} \in \partial\mathcal{D}^r \end{cases}. \quad (46)$$

From Eq. (46), the across-face solutions for interior faces, incident boundaries and reflecting boundaries have different meanings. For an interior face f ($\vec{r} \notin \partial\mathcal{D}$), the across-face solution comes from the cell K' . For incident boundaries ($\vec{r} \in \partial\mathcal{D}^d$), the across-face solution is a combination of integrals of the outgoing (ψ_m^-) and incident boundary fluxes (ψ_m^{inc}). Finally, for reflecting boundaries ($\vec{r} \in \partial\mathcal{D}^r$), the across-face solutions are simply the within-cell solutions. Therefore, the solution jump is exactly zero for all reflecting boundaries and yields no contribution to the error estimate.

With the error estimates defined for all cells $K \in \mathbb{T}_h^r$ for refinement level r , a criterion is needed to determine which cells should be refined. For this work, we choose to employ a refinement criterion of the following form,

$$\eta_K^r \geq \alpha \max_{K' \in \mathbb{T}_h^r} (\eta_{K'}^r), \quad (47)$$

where α is a user-defined value (0, 1). This refinement criterion has a simple meaning. If, for example, $\alpha = 0.2$, then a cell will be refined if its error estimate is greater than 20% of the cell with the largest error estimate. This does not necessarily mean that 80% of the mesh cells will be refined. Instead, the criterion simply states that any cell above a particular threshold will be refined.

6. Numerical Results

6.1. Exactly-Linear Transport Solutions

Our first numerical verification example demonstrates that the linear polygonal finite element basis functions capture an exactly-linear solution space. We will show this by the method of exact solutions (MES). We build our exact solution by investigating the 2D, $\frac{1}{2}$ energy group transport problem with no scattering and an angle-dependent distributed source,

$$\mu \frac{\partial \psi}{\partial x} + \eta \frac{\partial \psi}{\partial y} + \sigma_t \psi = Q(x, y, \mu, \eta), \quad (48)$$

where the streaming term was separated into the corresponding two-dimensional terms. We then define an angular flux solution that is linear in both space and angle along with the corresponding 0th-moment scalar flux ($\phi_{0,0} \rightarrow \phi$) solution:

$$\begin{aligned} \psi(x, y, \mu, \eta) &= ax + by + c\mu + d\eta + e \\ \phi(x, y) &= 2\pi(ax + by + e) \end{aligned} \quad (49)$$

Inserting the angular flux solution of Eq. (49) into Eq. (48) yields the following functional form for the distributed source:

$$Q(x, y, \mu, \eta) = a\mu + b\eta + \sigma_t(c\mu + d\eta) + \sigma_t(ax + by + e). \quad (50)$$

Our boundary conditions for all inflow boundaries are uniquely determined by the angular flux solution of Eq. (49). We test the barycentric functions on six different mesh types. These mesh types include triangular, quadrilateral, and polygonal meshes:

1. Orthogonal Cartesian mesh formed by the intersection of 11 equally-spaced vertices in both the x and y dimensions. This forms a 10x10 array of quadrilateral mesh cells.
2. Ordered-triangular mesh formed by the bisection of the previous orthogonal Cartesian mesh (forming 200 triangles all of the same size/shape).
3. Polygonal Shestakov grid formed by the randomization of vertices based on a skewness parameter [46, 47]. With a certain range of this skewness parameter, highly distorted meshes can be generated.
4. Sinusoidal polygonal grid that is generated by the transformation of a uniform orthogonal grid based on a sinusoid functional.
5. Kershaw's quadrilateral z-mesh [48]. This mesh is formed by taking an orthogonal quadrilateral grid and displacing certain interior vertices only in the y dimension.
6. A polygonal variant of the quadrilateral z-mesh.

The polygonal Shestakov grid, sinusoidal polygonal grid, and the polygonal z-mesh grid are formed by the conversion of an underlying quadrilateral grid into a corresponding polygonal grid by computing a bounded Voronoi diagram.

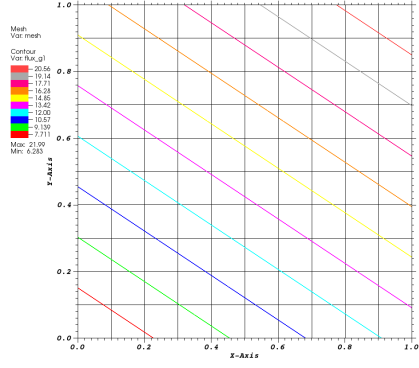
For this example, we set the function parameters to $\sigma_t = a = c = d = e = 1.0$ and $b = 1.5$. We gave the solution the 40% tilt in space ($a \neq b$) so that it would not align with the triangular mesh. Using an S_8 level-symmetric quadrature set [49], we ran all combinations of the barycentric basis functions and the mesh types. Figure 12 provides contour plots of the scalar flux solution for the Wachspress functions on the different meshes. We can see that an exactly-linear solution is captured as shown by the unbroken nature of the contour lines. The MV and ME functions provide identical results and are not shown for brevity.

6.2. Exactly-Quadratic Transport Solutions

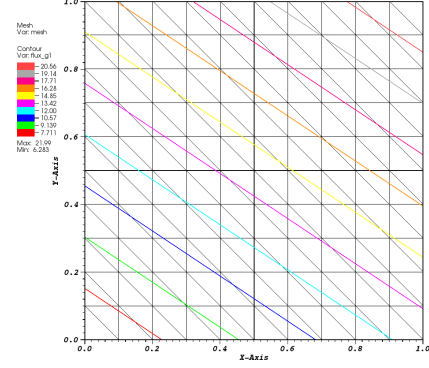
We next demonstrate that the quadratic serendipity basis functions capture the appropriate functional space with the hyperbolic transport equation. We will demonstrate this using two different MES solutions. The first problem interpolates the $\{1, x, y, x^2, xy, y^2\}$ span of functions, which we denote with the following exactly-quadratic spatial solution, $\{\psi_q, \phi_q\}$:

$$\begin{aligned} \psi_q(x, y, \mu, \eta) &= a + bx + cy + dxy + ex^2 + fy^2 \\ \phi_q(x, y) &= 2\pi(a + bx + cy + dxy + ex^2 + fy^2) \end{aligned} \quad (51)$$

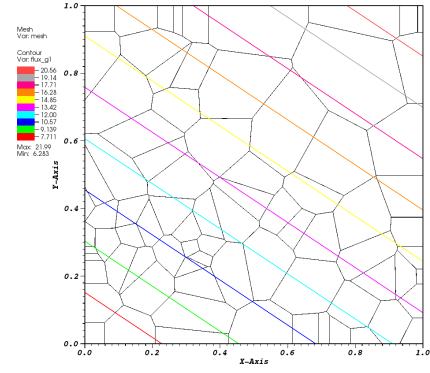
We clearly see that any combination of positive or negative (non-zero) values for the coefficients $a - f$ will span the quadratic serendipity space. The second



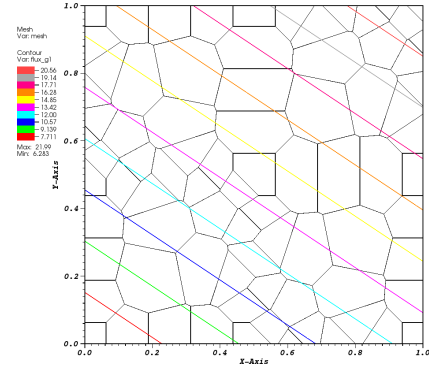
(a) Cartesian



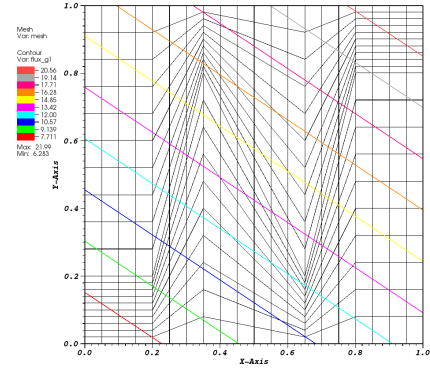
(b) Triangular



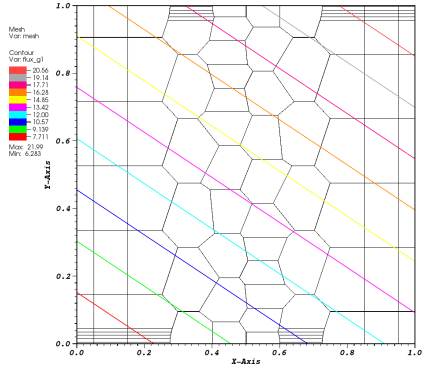
(c) Shestakov Polygons



(d) Sinusoid Polygons



(e) Z-Quadrilaterals



(f) Z-Polygons

Figure 12: Contour plots of the exactly-linear solution with the Wachspress basis functions.

454 problem contains terms up to x^2y^2 . This higher-order functional form has a
 455 solution, $\{\psi_{x2y2}, \phi_{x2y2}\}$, given by the following

$$\begin{aligned}\psi_{x2y2}(x, y, \mu, \eta) &= x(L_x - x)y(L_y - y) \\ \phi_{x2y2}(x, y) &= 2\pi x(L_x - x)y(L_y - y)\end{aligned}\tag{52}$$

456 where L_x and L_y are the dimensions of the domain in x and y . For this problem,
 457 we set $L_x = L_y = 1$.

458 From the methodology presented in Section 4, we expect the quadratic
 459 serendipity functions to exactly capture the ϕ_q solution but not the ϕ_{x2y2} so-
 460 lution. For both problems, we use the same meshes that were utilized for the
 461 exactly-linear problem in Section 6.1. Tables 2 and 3 give the L_2 -norm of the
 462 error for the quadratic and x^2y^2 solutions, respectively. We can clearly see from
 463 the machine precision results, that the quadratic serendipity functions exactly
 464 capture the ϕ_q solution. Likewise, the functions clearly do not capture the ϕ_{x2y2}
 465 solution.

Table 2: L_2 -norm of the error in the quadratic solution spanning $\{1, x, y, x^2, xy, y^2\}$ for the different quadratic serendipity basis functions on different mesh types.

	Basis Functions		
Mesh Type	Wachspress	Mean Value	Max. Entropy
Cartesian	2.23e-13	5.68e-14	5.65e-14
Triangular	7.85e-14	2.52e-14	2.54e-13
Shes. Poly	1.14e-14	5.75e-14	1.25e-13
Sine Poly	2.56e-13	3.25e-13	6.37e-13
Z-Quad	5.24e-14	1.68e-13	5.19e-14
Z-Poly	6.64e-14	8.29e-14	6.82e-13

Table 3: L_2 -norm of the error in the quadratic solution containing the x^2y^2 term for the different quadratic serendipity basis functions on different mesh types.

	Basis Functions		
Mesh Type	Wachspress	Mean Value	Max. Entropy
Cartesian	3.50e-06	8.29e-06	3.86e-05
Triangular	5.13e-05	5.13e-05	5.13e-05
Shes. Poly	3.97e-04	2.81e-04	3.91e-04
Sine Poly	3.75e-05	7.62e-05	1.39e-04
Z-Quad	2.93e-05	2.59e-05	3.46e-05
Z-Poly	2.98e-05	5.08e-05	1.17e-04

466 6.3. Convergence Rate Analysis by the Method of Manufactured Solutions

467 After verifying the interpolation space of the linear and quadratic serendipity functions, we now demonstrate that the functions capture the appropriate
 468 theoretical convergence rates using the **Method of Manufactured Solutions** [50].
 469 We demonstrate this on polygonal meshes generated by Voronoi diagrams in
 470 Section 6.3.1 and by polygonal meshes generated by spatial AMR in Section
 471 6.3.2.
 472

473 6.3.1. MMS on Voronoi Polygonal Meshes

474 For the first MMS example, we will analyze convergence rates on polygonal
 475 meshes generated from Voronoi diagrams. We use the PolyMesher mesh gen-
 476 erator [51] to generate all of our polygonal grids. The functional form of the
 477 MMS solution is a sinusoid, $\{\psi_s, \phi_s\}$, having the following parameterized form,

$$\begin{aligned}\psi_s(x, y) &= \sin(\nu \frac{\pi x}{L_x}) \sin(\nu \frac{\pi y}{L_y}), \\ \phi_s(x, y) &= 2\pi \sin(\nu \frac{\pi x}{L_x}) \sin(\nu \frac{\pi y}{L_y}),\end{aligned}\tag{53}$$

478 where ν is a frequency parameter ($\nu = 1, 2, 3, \dots$) that we have set to 3 for
 479 this problem. The domain is $[0, 1]^2$, which makes $L_x = L_y = 1$. The domain
 480 is filled with a pure absorber that has a total cross section of $\sigma_t = 1$. A S_8
 481 level-symmetric quadrature is used. Since the flux solution is exactly zero on
 482 all boundaries, vacuum boundary conditions can be employed everywhere.

483 We first provide examples of the polygonal meshes that are employed for this
 484 problem along with the corresponding MV isoline solutions in Figure 13. Upon
 485 convergence, PolyMesher provides grids with mesh cells composed of approxi-
 486 mately regular polygons. From the isolines, it is apparent that the quadratic
 487 functions better capture the sinusoid solution than the linear functions. This
 488 result is obvious since the curvature of the quadratic functions can better re-
 489 produce the smoothly varying nature of the sinusoid solution. Then, Figure 14
 490 provides the convergence rates for all of the functions in terms of the global
 491 number of degrees of freedom. The expected rates **of -1 and -3/2** are captured
 492 for the linear and quadratic functions, respectively.

493 6.3.2. MMS using Adaptive Mesh Refinement

494 For the second MMS example, we will analyze convergence rates on polygonal
 495 meshes generated from spatial AMR. The functional form of the MMS solution
 496 that will be analyzed is a localized Gaussian. This Gaussian solution space, $\{\psi_g,$
 497 $\phi_g\}$, that has its local maximum centered at (x_0, y_0) has the parameterized form,

$$\begin{aligned}\psi_g(x, y) &= C_M x(L_x - x)y(L_y - y) \exp(-\frac{(x - x_0)^2 + (y - y_0)^2}{\gamma}), \\ \phi_g(x, y) &= 2\pi C_M x(L_x - x)y(L_y - y) \exp(-\frac{(x - x_0)^2 + (y - y_0)^2}{\gamma}),\end{aligned}\tag{54}$$

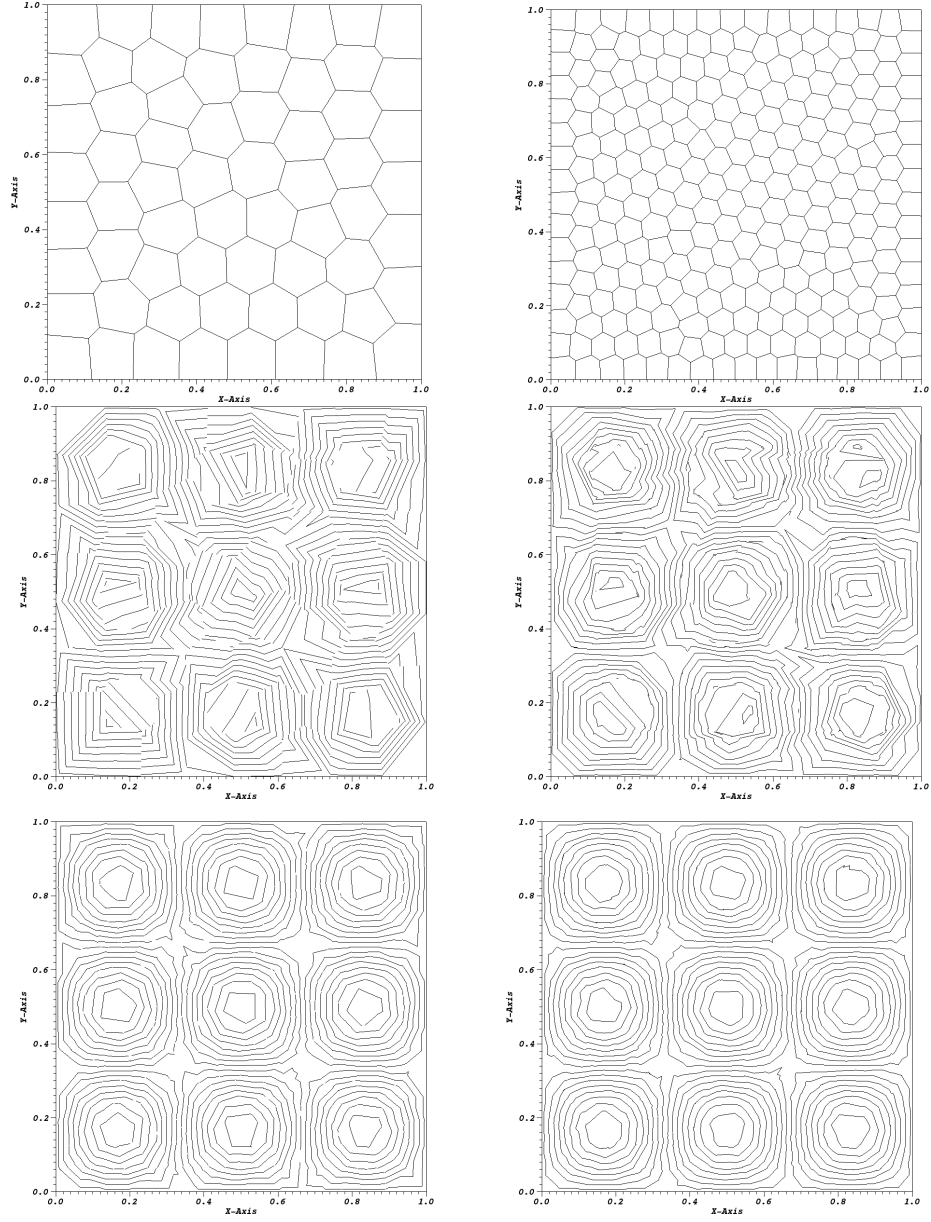


Figure 13: Examples contour plots of the sinusoid solution on polygonal meshes (top) using the linear mean value functions (middle) and the quadratic mean value functions (bottom).

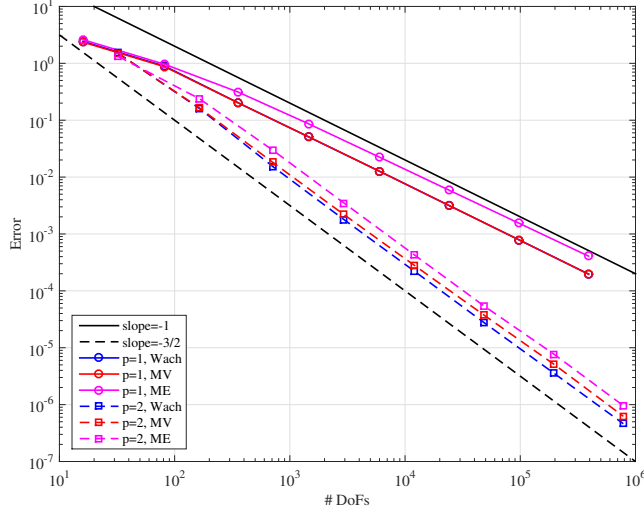


Figure 14: Convergence rates for the 2D Sinusoid MMS problem.

where the constants in the equations are:

$$C_M = \frac{100}{L_x^2 L_y^2} \quad \gamma = \frac{L_x L_y}{100}. \quad (55)$$

We again choose the dimensionality of our problem to be $[0, 1]^2$ which makes $L_x = L_y = 1$. We set the local maximum to be $x_0 = y_0 = 0.75$, which leads to a global maximum of $\frac{225}{32}\pi \approx 22.1$. The domain consists of a pure absorber with $\sigma_t = 1$ and the quadrature is again the S_8 level-symmetric set.

Because we are using AMR for this Gaussian problem, we will only analyze the MV and ME functions since the Wachspress functions cannot handle degenerate polygons. For both the linear and quadratic AMR runsets, the refinement criterion, α , was set to 0.1. Figure 15 gives the convergence history of the MMS error in the L_2 -norm. We plot the different AMR cases with their corresponding uniform refinement case ($\alpha = 0$) for comparison. We can clearly see that we obtain the proper convergence rates for all cases, and the AMR sets provide better solution accuracy with less spatial degrees of freedom. Finally, we provide an example of a pair of AMR meshes and solutions in Figure 16 using the ME basis functions. We can see a clear difference in how the linear and quadratic basis functions will refine, with the quadratic functions causing much smoother refinement to occur.

6.4. Convergence Rate Analysis Bounded by the Solution Regularity

Our next numerical example involves studying the convergence rates of transport solutions in a purely-absorbing medium. Specifically, we seek to analyze the effects of mesh alignment along the solution discontinuities for problems that will be constrained by the solution regularity. From Section 2, we noted

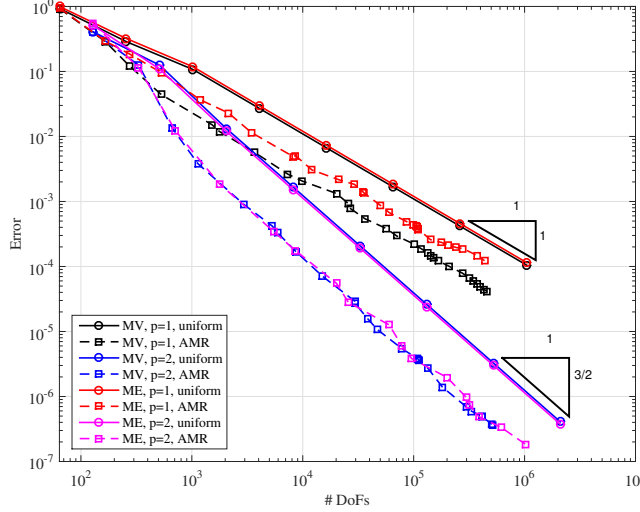


Figure 15: Convergence rates for the 2D Gaussian MMS problem.

that if the mesh does not align with the discontinuities of the transport solution, then the solution convergence is restricted by the regularity, r . However, if the mesh aligns with all of the solution discontinuities, then the maximum $p + 1$ convergence rates can be observed.

For this example, we analyze a transport problem without scattering ($\sigma_s = 0$) or a volumetric distributed source ($q = 0$). We will use a domain consisting of the unit square, $[0, 1]^2$, where an incident angular flux is imparted on the left face at a downward 45° angle. This means that there is a solution discontinuity along the line from the vertex $(0, 1)$ to $(1, 0)$ and the upper-right portion of the domain is a void. Therefore, this transport solution has a regularity of $1/2$.

Two different mesh types are analyzed for this example. The first mesh type is a polygonal mesh that is again generated with the PolyMesher software. The second mesh type is a split-polygonal mesh where the mesh elements that fall on the line $(0, 1)$ to $(1, 0)$ are bisected. This bisection aligns with the discontinuity of the transport solution. Therefore, we expect convergence of $1/2$ on the polygonal mesh and $p + 1$ on the split-polygonal mesh.

We first give an example solution of this problem on the two mesh types using the linear Wachspress functions in Figure 17. The solution does not "see" the transport discontinuity with the split-polygonal mesh, but the outflow boundaries on the polygonal mesh cause numerical dispersion across the transport discontinuity. The convergence rates in the L_2 -norm are given in Figures 18 and 19 for the split-polygonal and polygonal meshes, respectively. With the discontinuity-aligned, split-polygonal mesh, we can clearly see that convergence rates of $p + 1$ are obtained. With the polygonal mesh, we see that convergence rates of about $1/2$ are obtained for optically thin meshes. However, for thicker domains in the pre-asymptotic range, higher convergence rates (without quite

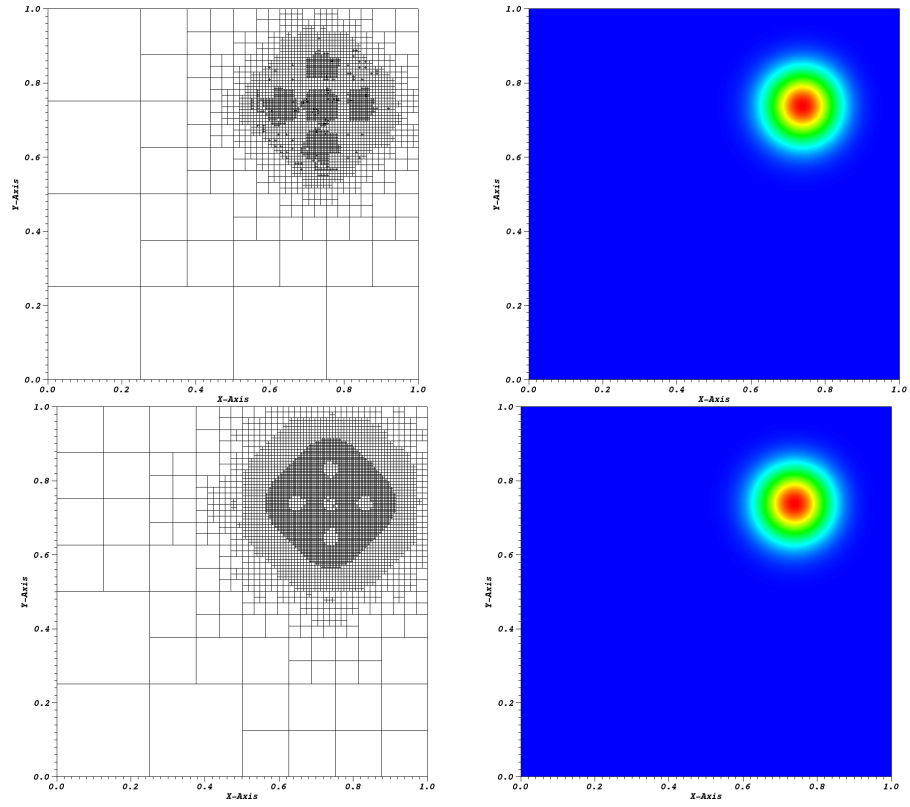


Figure 16: AMR meshes and solutions for the Gaussian MMS problem using the maximum entropy functions: (top) linear basis functions at cycle 15 and (bottom) quadratic serendipity basis functions at cycle 08.

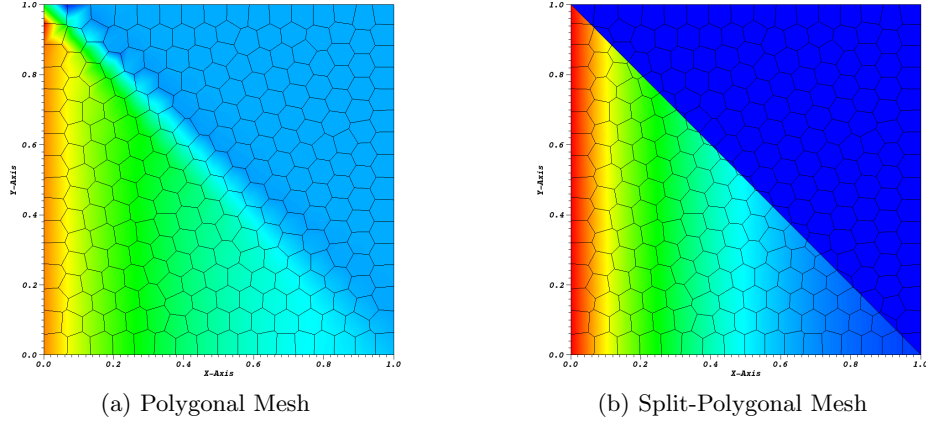


Figure 17: Example solution of the purely-absorbing medium case with left-face incidence and $\sigma_t = 1$ using the linear Wachspress basis functions.

obtaining $p + 1$ values) are observed.

6.5. *Thick Diffusive Problems*

So far, we have only presented numerical examples without scattering. Adams showed that the choice of spatial basis functions for the DGFEM transport equation is important in the thick diffusive limit [10]. We conclude our numerical examples by demonstrating the applicability of the linear and quadratic polygonal functions for optically thick transport problems that are dominated by scattering.

6.5.1. *1D-Analogue Unresolved Boundary Layer*

The first diffusive problem we will analyze is an unresolved boundary layer problem formed by an incident flux at a grazing angle. We again use a unit square domain $([0, 1]^2)$, where we use rectangular mesh cells with 10 cells in the x-dimension and 1 cell in the y-dimension. The top and bottom boundary faces are reflecting, the right boundary face is vacuum, and the left boundary face has an incident flux at the two extreme directions. A Product Gaussian-Legendre-Chebyshev (PGLC) angular quadrature [52] is used with 8 polar levels and 1 azimuthal level in an octant and where the polar axis is aligned with the x-axis. This quadrature set yields identical x-dimension cosines and weights to the 1D S_{16} Gauss-Legendre quadrature. Therefore, the incident flux grazing directions are $[0.09501250983763748, \pm 0.7039078856549176]$ with a value of $1/w$, where $w = 0.5951766460237447$. We note that the value of w is from the quadrature weights being normalized to 2π .

The total cross section is $\sigma_t = 500$ which makes the total mean free paths (mfp) of the problem also equal to 500. The domain is a pure scatterer ($\sigma_a = 0$) without a volumetric source. The scalar flux solutions are presented in Figure 20 along with a reference solution which is computed with the $\mathbb{Q}4$ functions

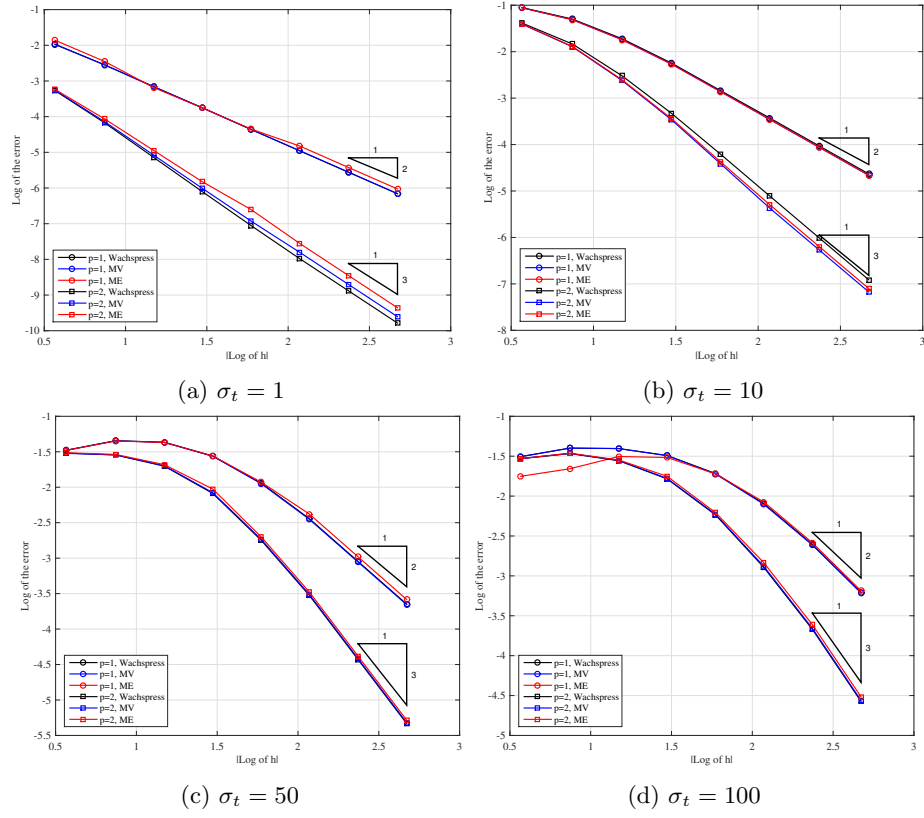


Figure 18: Convergence rates for the pure absorber problem with left-face incidence on split-polygonal meshes with different values of σ_t .

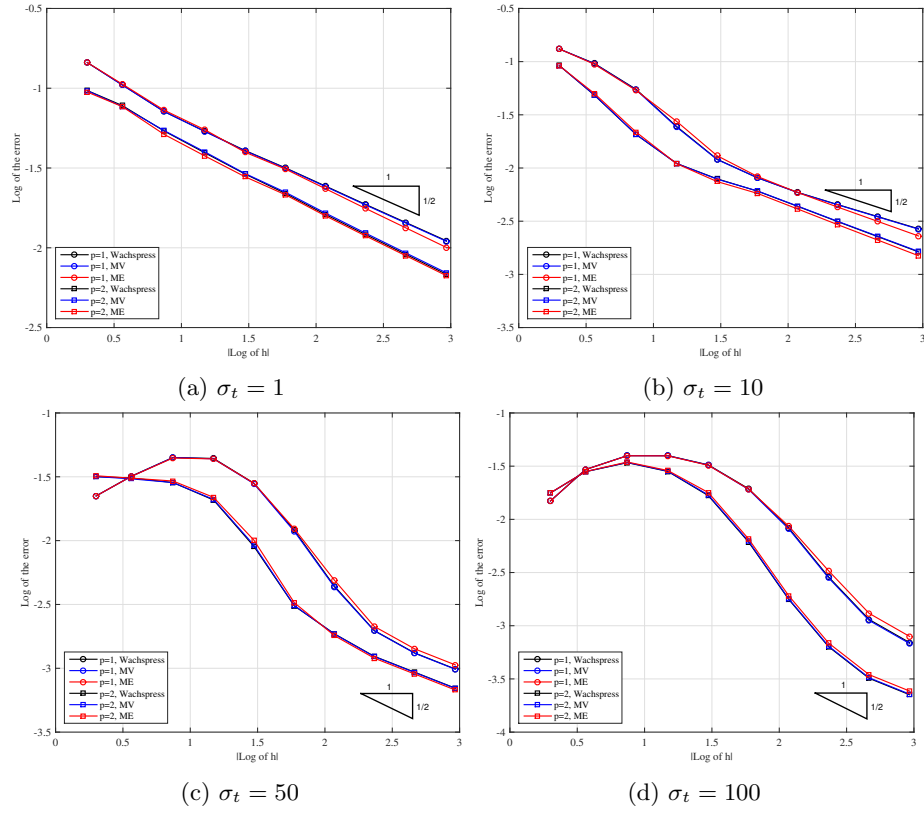


Figure 19: Convergence rates for the pure absorber problem with left-face incidence on polygonal meshes with different values of σ_t .

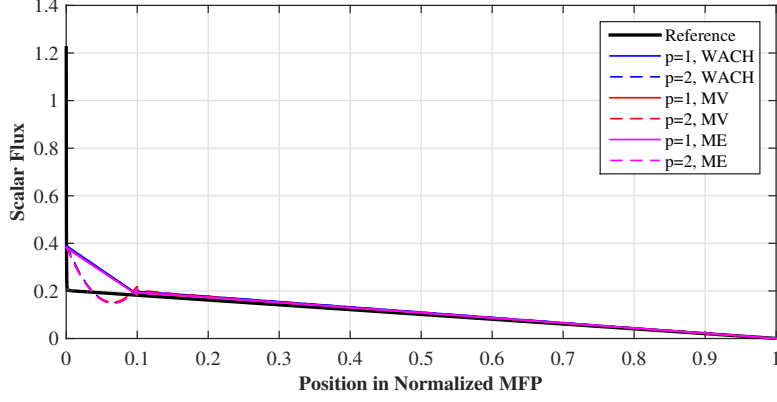


Figure 20: Scalar flux solution for the unresolved boundary layer problem.

572 on a mesh composed of 1000 spatial cells from $x \in [0, 0.01]$ and 1000 spatial
 573 cells from $x \in [0.01, 1]$. The reference solution mesh is also composed of only 1
 574 cell in the y-dimension. In Figure 20, we can see a strong boundary layer that
 575 rapidly drops from a value of about 1.25 to a value of about 0.21 within 0.5
 576 mfp lengths. The solution outflow from cell 1 is close to the reference outflow
 577 for all the linear and quadratic functions. The average scalar flux value of
 578 the reference solution for $x \in [0, 0.1]$ is about 0.189181. All of the linear and
 579 quadratic functions overpredict this average flux value, though the quadratic
 580 functions yield significantly closer values. These average flux values and their
 581 relative difference to the reference solution are given in Table 4.

Table 4: Average Value of the scalar flux from $x \in [0, 0.1]$ and the relative difference to the reference solution.

Basis Function	Degree	Average Value	Rel. % Difference
Wachspress	Linear	0.28216	49.15
	Quadratic	0.20757	9.72
Mean Value	Linear	0.28352	49.87
	Quadratic	0.21162	11.86
Maximum Entropy	Linear	0.28216	49.15
	Quadratic	0.20757	9.72

582 6.5.2. 2D Thick Diffusion Limit

583 The **second** diffusive problem that we will consider analyzes the thick dif-
 584 fusion limit of the transport equation. It consists of a homogeneous square
 585 domain $[0, 1]^2$ with isotropic scattering, an isotropic distributed source, and
 586 vacuum boundary conditions. The cross sections are scaled to reflect the prop-

erties of the thick diffusion limit [10]. If we introduce a scaling parameter, ϵ , then the total cross section, absorption cross section, and distributed source scale as $1/\epsilon$, ϵ , and ϵ , respectively. Using these scaled parameters yields transport and diffusion (standard) equations of

$$\vec{\Omega} \cdot \vec{\nabla} \psi + \frac{1}{\epsilon} \psi = \left(\frac{1}{\epsilon} - \epsilon \right) \frac{\phi}{4\pi} + \frac{\epsilon}{4\pi}, \quad (56)$$

and

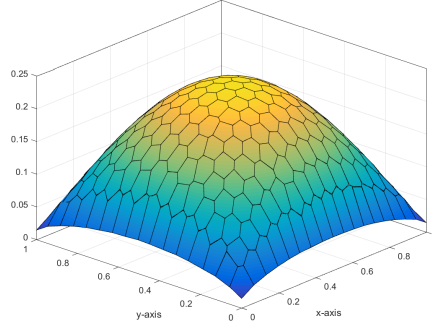
$$-\frac{\epsilon}{3} \nabla^2 \phi + \epsilon \phi = \epsilon, \quad (57)$$

respectively. We have kept the scaling terms in Equation 57 for completeness, even though the diffusion solution is invariant to the value of ϵ . The transport equation is discretized according to Eq. (5), while the diffusion equation is discretized using a continuous finite element method (CFEM) form. The diffusion equations use a homogeneous Dirichlet boundary condition, and the S_8 quadrature is used for the transport equations.

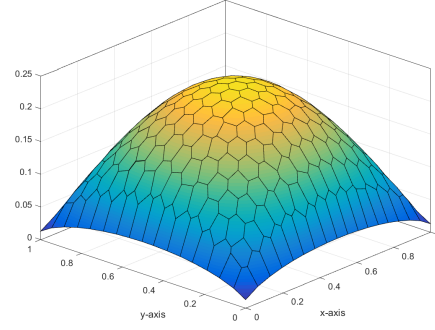
With the chosen boundary conditions, the transport and diffusion solutions will converge only as ϵ gets small. Specifically, they converge at a rate of $O(\epsilon)$ with any appropriate norm (we choose the L_2 -norm). Figure 21 provides the transport and diffusion solutions of the linear and quadratic maximum entropy functions. We can see that as ϵ goes from 10^{-1} to 10^{-5} , the transport solutions qualitatively converge to their corresponding diffusion solutions. Figure 22 then provides the convergence rates of the discretized transport, ϕ_T , and diffusion, ϕ_D , solutions under the L_2 -norm ($\|\phi_T - \phi_D\|_{L_2}$). We can see that the transport solution converges to the diffusion solution at a rate of ϵ , which is expected from [10].

7. Conclusions

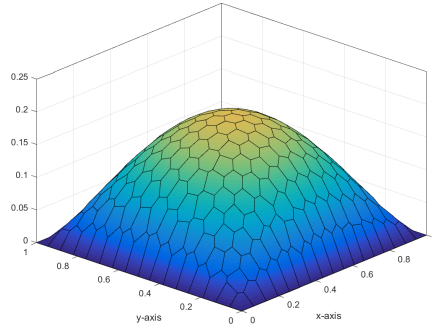
A higher-order discontinuous Galerkin finite element discretization using the quadratic serendipity space of functions has been applied to S_N transport equation on arbitrary polygonal grids. The quadratic serendipity functional space is formed by combinations of pairwise products of linear polygonal barycentric functions, of which we utilized the Wachspress functions, mean value functions, and maximum entropy functions in this work. The quadratic serendipity functions preserve the thick diffusion limit of the S_N transport equation as predicted by the theory of [10]. Third-order convergence was numerically verified for transport problems on polygonal grids that were not bound by the solution regularity. Asymptotic convergence rates of $1/2$ were appropriately obtained for problems where the employed meshes caused the transport solutions to live in the $H^{1/2}(\mathcal{D})$ Hilbert space. Spatial adaptive mesh refinement was also used to solve the transport equation on polygonal grids. Hanging nodes were eliminated and cells adjacent to refined cells with common edges were treated as degenerate polygons with collinear vertices. We verified that third-order convergence was



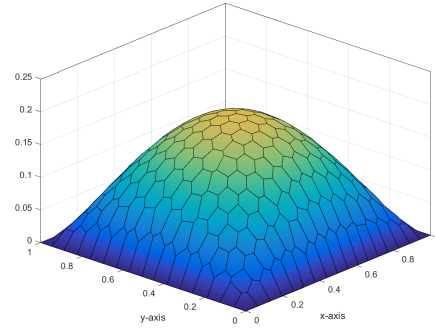
(a) Linear, $\epsilon = 10^{-1}$



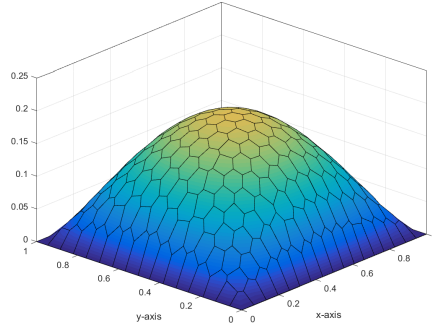
(b) Quadratic, $\epsilon = 10^{-1}$



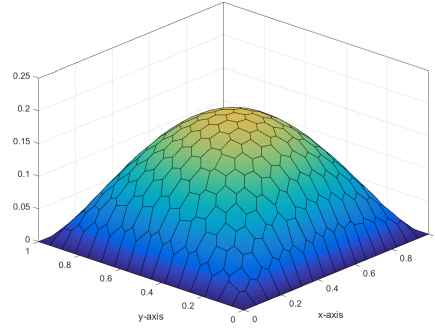
(c) Linear, $\epsilon = 10^{-5}$



(d) Quadratic, $\epsilon = 10^{-5}$



(e) Linear, Diffusion



(f) Quadratic, Diffusion

Figure 21: Solutions of the thick diffusion limit problem using the maximum entropy basis functions. The top and middle rows show the linear and quadratic transport solutions for $\epsilon = 10^{-1}$ and $\epsilon = 10^{-5}$, respectively. The bottom row shows the corresponding diffusion solutions.

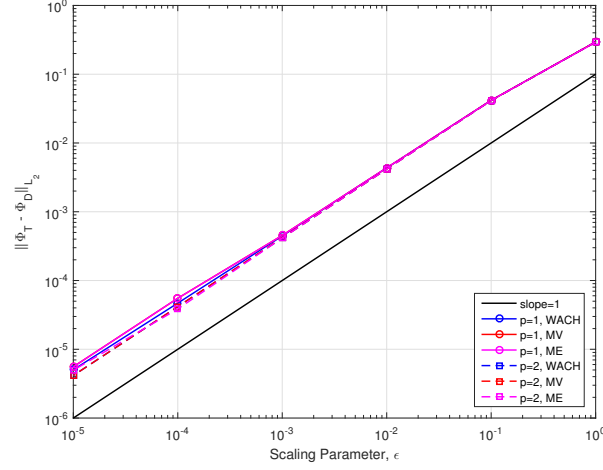


Figure 22: Convergence rates for the diffusion limit problem on a polygonal mesh.

retained while achieving greater solution accuracy with fewer unknowns than grids that were uniformly refined.

This paper shows that the S_N transport equation can be effectively discretized on arbitrary polygonal meshes using a higher-order DGFEM spatial discretization. However, we are not constrained to just the first order form of the S_N transport equation. The basis functions presented here can be employed with other forms of the transport equation including the self-adjoint angular flux equation, the least-squares equation, and the even-parity equations, as well as the P_N method in angle. Furthermore, these basis functions can be employed with a CFEM discretization of the transport equation.

References

- [1] James J Duderstadt and William Russell Martin. *Transport theory*. John Wiley & Sons, 1979.
- [2] Wm H Reed and TR Hill. Triangular mesh methods for the neutron transport equation. *Los Alamos Report LA-UR-73-479*, 1973.
- [3] P Lesaint and Pierre-Arnaud Raviart. On a finite element method for solving the neutron transport equation. *Mathematical aspects of finite elements in partial differential equations*, (33):89–123, 1974.
- [4] ML Adams and EW Larsen. Fast iterative methods for discrete-ordinates particle transport calculations. *Progress in nuclear energy*, 40(1):3–159, 2002.
- [5] William Daryl Hawkins, Timmie Smith, Michael P Adams, Lawrence Rauchwerger, Nancy M Amato, and Marvin L Adams. Efficient massively

- parallel transport sweeps. In *Transactions of the American Nuclear Society*, volume 107, pages 477–481, 2012.
- [6] Thomas M Evans, Alissa S Stafford, Rachel N Slaybaugh, and Kevin T Clarno. Denovo: A new three-dimensional parallel discrete ordinates code in scale. *Nuclear technology*, 171(2):171–200, 2010.
- [7] RE Alcouffe, RS Baker, JA Dahl, and SA Turner. Partisn code abstract. In *PHYSOR 2000 International Topical Meeting, Advances in Reactor Physics and Mathematics and Computation into the Next Millenium*, 2000.
- [8] Todd A Wareing, John M McGhee, and Jim E Morel. Attila: A three-dimensional, unstructured tetrahedral mesh discrete ordinates transport code. In *Transactions of the American Nuclear Society*, volume 75, 1996.
- [9] M.D. DeHart. Newt: A new transport algorithm for two-dimensional discrete ordinates analysis in non-orthogonal geometries. Technical report, ORNL, 2006.
- [10] Marvin L Adams. Discontinuous finite element transport solutions in thick diffusive problems. *Nuclear science and engineering*, 137(3):298–333, 2001.
- [11] Wm H Reed, TR Hill, FW Brinkley, and KD Lathrop. Triplet: A two-dimensional, multigroup, triangular mesh, planar geometry, explicit transport code. Technical report, Los Alamos Scientific Lab., N. Mex.(USA), 1973.
- [12] Yaqi Wang and Jean C Ragusa. On the convergence of dgfm applied to the discrete ordinates transport equation for structured and unstructured triangular meshes. *Nuclear Science and Engineering*, 163(1):56–72, 2009.
- [13] Yaqi Wang and Jean C Ragusa. A high-order discontinuous galerkin method for the s_n transport equations on 2d unstructured triangular meshes. *Annals of Nuclear Energy*, 36(7):931–939, 2009.
- [14] Yousry Y Azmy. The weighted diamond-difference form of nodal transport methods. *Nuclear Science & Engineering*, 98(1):29–40, 1988.
- [15] Yousry Y Azmy. Arbitrarily high order characteristic methods for solving the neutron transport equation. *Annals of Nuclear Energy*, 19(10-12):593–606, 1992.
- [16] EL Wachspress. High-order curved finite elements. *International Journal for Numerical Methods in Engineering*, 17(5):735–745, 1981.
- [17] STAR-CCM+. <http://www.cd-adapco.com>. 2015.
- [18] Mien Yip, Jon Mohle, and JE Bolander. Automated modeling of three-dimensional structural components using irregular lattices. *Computer-Aided Civil and Infrastructure Engineering*, 20(6):393–407, 2005.

- [19] Alexander Rand, Andrew Gillette, and Chandrajit Bajaj. Quadratic serendipity finite elements on polygons using generalized barycentric coordinates. *Mathematics of computation*, 83(290):2691–2716, 2014.
- [20] JE Morel and JM McGhee. A self-adjoint angular flux equation. *Nuclear science and engineering*, 132(3):312–325, 1999.
- [21] RT Ackroyd. Least-squares derivation of extremum and weighted-residual methods for equations of reactor physics. *Annals of Nuclear Energy*, 10(2):65–99, 1983.
- [22] EE Lewis. Finite element approximation to the even-parity transport equation. In *Advances in Nuclear Science and Technology*, pages 155–225. Springer, 1981.
- [23] CRE de Oliveira and AJH Goddard. Event - a multidimensional finite element-spherical harmonics radiation transport code. In *Proc. OECD Int. Sem. 3D Deterministic Radiation Transport Codes*, 1996.
- [24] FN Gleicher, Y Wang, D Gaston, and R Martineau. The method of manufactured solutions for rattlesnake, a s_n radiation transport solver inside the moose framework. volume 106, pages 372–374. American Nuclear Society, 2012.
- [25] Paul Houston, Christoph Schwab, and Endre Süli. Stabilized hp-finite element methods for first-order hyperbolic problems. *SIAM Journal on Numerical Analysis*, 37(5):1618–1643, 2000.
- [26] Paul Houston, Christoph Schwab, and Endre Süli. Discontinuous hp-finite element methods for advection-diffusion-reaction problems. *SIAM Journal on Numerical Analysis*, 39(6):2133–2163, 2002.
- [27] Douglas N Arnold and Gerard Awanou. The serendipity family of finite elements. *Foundations of Computational Mathematics*, 11(3):337–344, 2011.
- [28] N Sukumar and EA Malsch. Recent advances in the construction of polygonal finite element interpolants. *Archives of Computational Methods in Engineering*, 13(1):129–163, 2006.
- [29] Eugene L Wachspress. A rational finite element basis. *Mathematics in science and engineering*, 1975.
- [30] Michael S Floater. Mean value coordinates. *Computer aided geometric design*, 20(1):19–27, 2003.
- [31] N Sukumar. Construction of polygonal interpolants: a maximum entropy approach. *International Journal for Numerical Methods in Engineering*, 61(12):2159–2181, 2004.
- [32] Claude Elwood Shannon. A mathematical theory of communication. *Bell Systems Technical Journal*, 27:379–423, 1948.

- 722 [33] Edwin T Jaynes. Information theory and statistical mechanics. *Physical*
723 *review*, 106(4):620–630, 1957.
- 724 [34] Stephen Boyd and Lieven Vandenbergh. *Convex optimization*. Cambridge
725 university press, 2004.
- 726 [35] David González, Elías Cueto, and Manuel Doblaré. A higher order method
727 based on local maximum entropy approximation. *International journal for*
728 *numerical methods in engineering*, 83(6):741–764, 2010.
- 729 [36] N Sukumar. Quadratic maximum-entropy serendipity shape functions for
730 arbitrary planar polygons. *Computer Methods in Applied Mechanics and*
731 *Engineering*, 263:27–41, 2013.
- 732 [37] Roger Penrose. A generalized inverse for matrices. In *Mathematical pro-*
733 *ceedings of the Cambridge philosophical society*, volume 51, pages 406–413.
734 Cambridge Univ Press, 1955.
- 735 [38] Christian Führer and Guido Kanschat. A posteriori error control in radia-
736 tive transfer. *Computing*, 58(4):317–334, 1997.
- 737 [39] Andreas Dedner and Peter Vollmöller. An adaptive higher order method
738 for solving the radiation transport equation on unstructured grids. *Journal*
739 *of Computational Physics*, 178(2):263–289, 2002.
- 740 [40] Ralf Hartmann and Paul Houston. Adaptive discontinuous galerkin finite
741 element methods for nonlinear hyperbolic conservation laws. *SIAM Journal*
742 *on Scientific Computing*, 24(3):979–1004, 2003.
- 743 [41] Yaqi Wang and Jean C Ragusa. Standard and goal-oriented adaptive mesh
744 refinement applied to radiation transport on 2d unstructured triangular
745 meshes. *Journal of Computational Physics*, 230(3):763–788, 2011.
- 746 [42] Rüdiger Verfürth. *A review of a posteriori error estimation and adaptive*
747 *mesh-refinement techniques*. John Wiley & Sons Inc, 1996.
- 748 [43] Mark Ainsworth and J Tinsley Oden. *A posteriori error estimation in finite*
749 *element analysis*, volume 37. John Wiley & Sons, 2011.
- 750 [44] Ralf Hartmann. *Adaptive finite element methods for the compressible euler*
751 *equations*. PhD thesis, University of Heidelberg, 2002.
- 752 [45] Leszek Demkowicz. *Computing with hp-Adaptive Finite Elements: Volume*
753 *1 One and Two Dimensional Elliptic and Maxwell problems*. CRC Press,
754 2006.
- 755 [46] AI Shestakov, JA Harte, and DS Kershaw. Solution of the diffusion equa-
756 tion by finite elements in lagrangian hydrodynamic codes. *Journal of Com-*
757 *putational Physics*, 76(2):385–413, 1988.

- [47] AI Shestakov, DS Kershaw, and GB Zimmerman. Test problems in radiative transfer calculations. *Nuclear science and engineering*, 105(1):88–104, 1990.
- [48] David S Kershaw. Differencing of the diffusion equation in lagrangian hydrodynamic codes. *Journal of Computational Physics*, 39(2):375–395, 1981.
- [49] Elmer Eugene Lewis and Warren F Miller. *Computational methods of neutron transport*. John Wiley and Sons, Inc., New York, NY, 1984.
- [50] Kambiz Salari and Patrick Knupp. Code verification by the method of manufactured solutions. Technical report, Sandia National Labs., Albuquerque, NM (US); Sandia National Labs., Livermore, CA (US), 2000.
- [51] Cameron Talischi, Glaucio H Paulino, Anderson Pereira, and Ivan FM Menezes. Polymesher: a general-purpose mesh generator for polygonal elements written in matlab. *Structural and Multidisciplinary Optimization*, 45(3):309–328, 2012.
- [52] IK Abu-Shumays. Compatible product angular quadrature for neutron transport in xy geometry. *Nuclear Science and Engineering*, 64(2):299–316, 1977.

A. Limits of the Barycentric Functions on the Boundary

Each of the three basis functions presented in this paper satisfies the definitions of the general barycentric functions given in Section 3. These three function spaces can be written for a polygonal element K with n vertices using the general form:

$$\lambda_i(\vec{r}) = \frac{w_i(\vec{r})}{\sum_{j=1}^n w_j(\vec{r})}. \quad (58)$$

The differences between the three functions lie with the definition of the weight functions, w . Unfortunately, for each function space, there is a sub-set of the element boundary, ∂K , where some of the weight functions are undefined (divide-by-zero numerical evaluations). However, these functions do have valid limits, which can be directly evaluated to compute the surface integrals in Eq. (5). For this analysis, we will evaluate the limits of the barycentric functions on face e_j connected by vertices j and $j + 1$.

$$\lim_{\vec{r} \rightarrow \vec{r}^* \in e_j} \lambda_j(\vec{r}) = \frac{w_j(\vec{r})}{w_j(\vec{r}) + w_{j+1}(\vec{r})} \quad (59)$$

and

$$\lim_{\vec{r} \rightarrow \vec{r}^* \in e_j} \lambda_{j+1}(\vec{r}) = \frac{w_{j+1}(\vec{r})}{w_j(\vec{r}) + w_{j+1}(\vec{r})}, \quad (60)$$

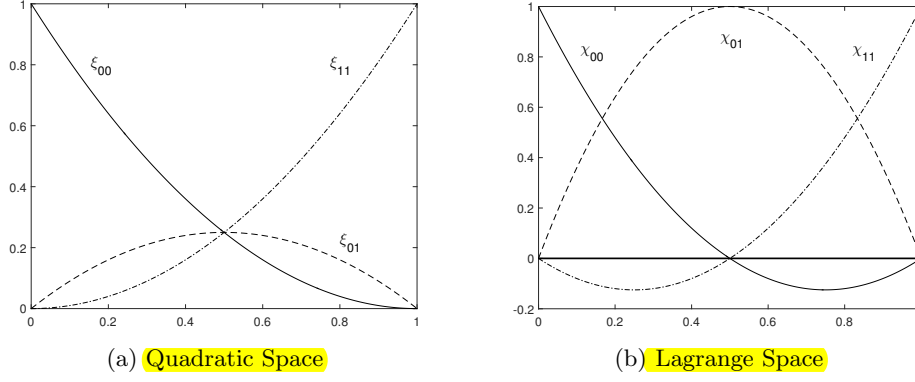


Figure 23: Comparison on a polygonal face of the quadratic basis (left) and the standard Lagrange basis (right).

respectively.

$$w_j(\vec{r})(\vec{r}_j - \vec{r}) + w_{j+1}(\vec{r})(\vec{r}_{j+1} - \vec{r}) = \vec{0}. \quad (61)$$

If we take the norm of Eq. (61) and rearrange terms, then we obtain

$$\frac{w_{j+1}}{w_j} = \frac{|\vec{r}_j - \vec{r}|}{|\vec{r}_{j+1} - \vec{r}|}. \quad (62)$$

If we appropriately insert Eq. (62) into Eqs. (59) and (60), then we obtain a final expression for the limit of the barycentric functions on face e_j :

$$\lim_{\vec{r} \rightarrow \vec{r}^* \in e_j} \lambda_i(\vec{r}) = \begin{cases} \frac{|\vec{r}_{j+1} - \vec{r}|}{|\vec{r}_{j+1} - \vec{r}_j|}, & i = j \\ \frac{|\vec{r}_j - \vec{r}|}{|\vec{r}_{j+1} - \vec{r}_j|}, & i = j + 1 \\ 0, & \text{otherwise} \end{cases} \quad (63)$$

From Eq. (63), we can see that the Lagrange property and the piecewise boundary linearity property are satisfied. Using the limits of λ_j and λ_{j+1} on face e_j , we can explicitly write the surface integral as

$$\langle \vec{n} b, b \rangle_{e_j} = \frac{L_j \vec{n}_j}{6} \begin{bmatrix} 2 & 1 \\ 1 & 2 \end{bmatrix}, \quad (64)$$

where $b = [b_j, b_{j+1}]$, \vec{n}_j is the normal direction of face e_j , and L_j is the length of face e_j .

B. Conversion of the Serendipity Functions to the Lagrange Space

The serendipity functions are formed from the pairwise products of vertex-based linear functions. Therefore, these functions will not satisfy the Lagrange property like their linear parent functions as can be seen in Figure 23a along an

801 arbitrary polygonal face. We can convert the quadratic serendipity functions
 802 to a Lagrange basis, $\{\chi(\vec{r})\}$, which have the same functional form as the \mathbb{Q}_9
 803 functions on a face as seen in Figure 23b. The Lagrange basis spans the same
 804 functional space as the quadratic serendipity functions, $\{1, x, y, x^2, xy, y^2\}$, and
 805 is formed by:

$$\chi_{ii} = \xi_{ii} - \xi_{i,i+1} - \xi_{i-1,i} \quad \text{and} \quad \chi_{i,i+1} = 4\xi_{i,i+1}. \quad (65)$$

806 We can see from Eq. (65) that the Lagrange functions are a linear combination of
 807 the quadratic serendipity functions, which we can formally define as $\{\chi\} = \mathbb{L}\{\xi\}$.
 808 The transformation matrix, \mathbb{L} , has a simple structure as seen in Eq. (66).

$$\mathbb{L} = \left[\begin{array}{ccccc|ccccc} 1 & & & & & -1 & 0 & \dots & 0 & -1 \\ & \ddots & & & & -1 & -1 & 0 & \dots & 0 \\ & & \ddots & & & 0 & \ddots & \ddots & \ddots & \vdots \\ & & & \ddots & & \vdots & \ddots & \ddots & \ddots & 0 \\ & & & & 1 & 0 & \dots & 0 & -1 & -1 \\ \hline & & & & & 4 & & & & \\ & & 0 & & & & \ddots & & & \\ & & & & & & & \ddots & & \\ & & & & & & & & \ddots & \\ & & & & & & & & & 4 \end{array} \right] \quad (66)$$